Monthly Notices of the ROYAL ASTRONOMICAL SOCIETY
MNRAS **550**, 1–18 (2026)
Advance Access publication 2026 July 10
https://doi.org/10.1093/mnras/stag1287

Reproducing stellar structures in the Magellanic Clouds using a genetic algorithm with N-body simulations

Bethany R. Garver [1]★ David L. Nidever [1,2] Victor P. Debattista [3]★ and Nathan Deg [4]
[1]*Department of Physics, Montana State University, P.O. Box 173840, Bozeman, MT 59717-3840, USA*
[2]*Center for Computational Astrophysics, Flatiron Institute, 162 Fifth Avenue, New York, NY 10010, USA*
[3]*Jeremiah Horrocks Institute, University of Lancashire, Preston PR1 2HE, UK*
[4]*Department of Physics, Engineering Physics, and Astronomy, Queen's University, Kingston ON K7L 3N6, Canada*

Accepted 2026 July 3. Received 2026 July 2; in original form 2026 February 4

ABSTRACT
The Large and Small Magellanic Clouds (LMC and SMC, respectively) are the largest satellite galaxies of the Milky Way (MW) and their interactions with each other have given rise to multiple stellar substructures in their periphery as well as the gaseous Magellanic Stream. To better understand the origin of the stellar substructures and constrain their past orbit, we model the past 2.5 Gyr of the interactions between the MW and the LMC and SMC using N-body simulations. Due to the strong interactions, analytical orbit integrations are insufficient to analyse the past galaxy orbits accurately. Therefore, we use a genetic algorithm in combination with N-body simulations to determine the LMC and SMC initial positions and velocities 2.5 Gyr ago that result in the Magellanic Clouds (MCs) arriving near their observed locations and velocities at the current time. After running ∼8000 simulations, our best matching model includes two close interactions between the MCs (940 and 140 Myr ago) and reproduces some observed features of the MCs, including the LMC disc warp, a ring-shaped overdensity in the LMC, the tidal expansion of the SMC, and a greater distance dispersion on the eastern side of the SMC. The LMC disc warp is caused by the most recent interaction with the SMC, which occurred ∼140 Myr before the present. The interaction causes global ripples in the LMC disc with a mean amplitude of 1.3 kpc.

Key words: galaxies: dwarf – galaxies: interactions – Magellanic Clouds.

1 INTRODUCTION

The Large Magellanic Cloud (LMC) and Small Magellanic Cloud (SMC) are nearby galaxies interacting with each other and with the Milky Way (MW). Their structure has been studied for decades with optical and near-infrared (NIR) photometry (e.g. R. P. der Marel 2001; A. D. Mackey et al. 2016; D. L. Nidever et al. 2017), optical/NIR spectroscopy (e.g. R. P. der Marel et al. 2002; R. Carrera et al. 2008; D. L. Nidever et al. 2020), UV (L. M. Z. Hagen et al. 2017), Hα (K. A. Barger, L. M. Haffner & J. Bland-Hawthorn 2013), radio continuum (e.g. U. Klein et al. 1993; M. D. Filipovic et al. 1998), molecular gas (e.g. T. Wong et al. 2011), 21cm HI (e.g. M. E. Putman et al. 2003; D. L. Nidever, S. R. Majewski & W. Butler Burton 2008), and more.

Recent wide-field surveys and spectroscopic studies have revealed that the Magellanic Clouds host a wealth of substructure, providing strong evidence of their dynamic interaction history. S. R. Majewski et al. (2009) and D. L. Nidever et al. (2011) used pencil-beam Washington+*DDO*51 photometry with follow-up spectroscopy of giant stars to discover evidence for very extended stellar components around the MCs (LMC: $R \approx 20^\circ$, SMC: $R \approx 12^\circ$). A. Saha et al. (2010) used deep photometry to track main-sequence turnoff stars out to a radius of $\sim 16^\circ$ to the north. A. D. Mackey et al. (2016) first mapped the northern stream of the LMC, and subsequent work with deeper imaging revealed that this structure extends even farther (V. A. Belokurov & D. Erkal 2019) and includes two distinctive southern 'hook'-shaped features (D. Mackey et al. 2018). Using red clump stars from the Survey of the Magellanic Stellar History (SMASH; D. L. Nidever et al. 2017, 2021), Y. Choi et al. (2018a, b) mapped the three-dimensional geometry of the LMC disc and uncovered a pronounced southern warp extending roughly 4 kpc below the disc plane in the direction of the SMC. S. Saroon & S. Subramanian (2022) later identified a northern warp with *Gaia* DR2 data that bends in the same direction, giving the LMC disc a 'U'-shaped morphology – an unexpected feature if the distortion were purely tidal in origin. In addition, the outer stellar density profile of the LMC shows significant irregularities. D. L. Nidever et al. (2019a) found that while the overall profile can be described by a double-exponential or exponential-plus-power-law form, there is considerable scatter about the best-fitting model, indicating substantial substructure in the outskirts. Kinematically, K. A. G. Olsen et al. (2011) uncovered a population of metal-poor, counter-rotating stars in the LMC, providing further evidence for past interactions or accretion events. Finally, D. L. Nidever et al. (2020) used SDSS-IV/APOGEE-2S (S. R. Majewski et al. 2017)

★ E-mail: bethanygarver@montana.edu (BRG); vpdebattista@lancashire.ac.uk (VPD)

high-resolution spectroscopy to map the chemical enrichment of both Clouds, finding similarly low [α/Fe] 'knees' at [Fe/H] ≈ -2.2 and evidence for recent starburst activity, further linking the Clouds' chemical evolution to their dynamical interaction history.

The SMC exhibits a similarly complex structure, with both its morphology and kinematics bearing clear signatures of tidal influence from the LMC. Early photographic studies revealed a distance bimodality in the eastern SMC (D. Hatzidimitriou & M. R. S. Hawkins 1989), later confirmed with deep photometric data by D. L. Nidever et al. (2013), who found that the more distant eastern component resembles the central and western regions of the SMC, while the nearer eastern component consists of tidally stripped material. Spectroscopic evidence supports this picture with A. Almeida et al. (2024) showing that the distant eastern stars have a metallicity distribution function (MDF) similar to that of the western population, whereas the near eastern stars are more metal-rich, resembling the central SMC population – consistent with their origin as recently stripped stars. C. E. Murray et al. (2024) investigated young massive stars in the SMC and found that the galaxy contains two distinct star-forming systems separated by $\sim$5 kpc along the line of sight. The SMC also possesses extended stellar features, including the SMC Northern Overdensity (SMCNOD), discovered by A. Pieres et al. (2017) using DES data (Dark Energy Survey Collaboration 2016), located roughly 8° from the SMC centre. The timing and geometry of these features provide important constraints on the most recent close encounter between the Clouds. Y. Choi et al. (2022) used *Gaia* measurements of LMC disc distortions to infer the timing and impact parameter of this interaction and found that it likely occurred $\sim$140–160 Myr ago with an impact parameter of $\sim$5 kpc. Observational constraints from *Gaia* DR2, including proper motions and radial velocities of red giant stars, were used by P. Zivick, N. Kallivayalil & R. P. van der Marel (2021) to model SMC kinematics, revealing a modest intrinsic rotation of $\sim$10–20 km s^{-1} and a tidal expansion component of $\sim$10 km s^{-1} kpc^{-1}. P. Massana, D. L. Nidever & K. Olsen (2024) used *Gaia* XP stellar parameters from R. Andrae, H.-W. Rix & V. Chandra (2023) to map metallicities across the MCs and found that both the SMCNOD and its southern counterpart, the SMCSOD, are metal-poor with MDFs similar to those in the SMC outskirts. V. Ripepi et al. (2017) identified the SMC's elongated (or broken) structure, which was reproduced in simulations by J. Wang et al. (2019). Together, these discoveries paint a picture of a dynamically active Magellanic system, where repeated interactions between the LMC and SMC have produced tidal warps, streams, and extended stellar envelopes.

Simulations of the Magellanic Clouds have progressed from early low-resolution N-body approaches (e.g. D. N. C. Lin & D. Lynden-Bell 1977; W. E. Kunkel 1979; T. Murai & M. Fujimoto 1980) to modern hydrodynamical models that incorporate detailed Milky Way interactions and internal cloud dynamics. A. Růžička, C. Theis & J. Palouš (2010) performed a broad parameter-space search using a genetic algorithm (M. Wahde 1998; C. Theis 1999) with test-particle simulations, providing some initial constraints on the orbital and interaction history of the Clouds. T. W. Connors, D. Kawata & B. K. Gibson (2006) N-body simulations reproduced the Leading Arm and the two filaments of the trailing Stream using tidal interactions between the MCs and MW in a scenario where the MCs are on their second passage with the MW. R. Chisholm et al. (2025) modelled the pre-infall LMC–SMC system analogue in a cosmological simulation and reproduced the Magellanic Stream, Magellanic Bridge, and Leading Arm. After G. Besla et al. (2007) discovered that the MCs are very likely on their first infall into the MW, a newer generation of simulations by G. Besla et al. (2012) and J. D. Diaz & K. Bekki (2012) explored the interactions between the LMC and SMC and were able to reproduce key features of the Magellanic Stream, including its bifurcated filamentary structure and predicted the SMC 'counterbridge'. J. D. Diaz & K. Bekki (2012) included a previous close passage between the MCs and MW in their simulation. H. Rathore et al. (2025a, b, 2026) found that an interaction between the MCs $\sim$150 Myr ago would help explain the LMC's bar, LMC warp, SMC line-of-sight depth, and SMC tidal expansion.

Hydrodynamical simulations have further illuminated the role of gas physics in shaping the Magellanic system. S. Lucchini et al. (2020) included a hot Magellanic corona in their models, which shields leading gas from ram pressure stripping by the MW halo and naturally produces the observed Leading Arm Feature (LAF; M. E. Putman et al. 1998; C. Brüns et al. 2005). J. Wang et al. (2019) reproduced several features of the Magellanic Stream, including two filamentary substructures that originate from the LMC and SMC, respectively. While S. Lucchini, E. D'Onghia & A. J. Fox (2021) suggested that the trailing Magellanic Stream could lie as close as $\sim$20 kpc, recent stellar detections within the Stream at $\sim$100 kpc (D. Zaritsky et al. 2020; V. Chandra et al. 2023) indicate a greater distance. Supporting these models, A. M. Price-Whelan et al. (2019) and D. L. Nidever et al. (2019b) identified a young (117 Myr) star cluster in the MW formed from Leading Arm gas.

Comprehensive simulation suites such as KRATOS (Ó. Jiménez-Arranz et al. 2024b), and the studies by Y. Sheng et al. (2024) and S. Lucchini, E. D'Onghia & A. J. Fox (2024) explore a wide range of parameters including halo masses, corona properties, and orbital histories, providing frameworks to reproduce both the large-scale gaseous features and the complex stellar substructures observed today. Additionally, E. Vasiliev (2024) demonstrated methods for evolving an LMC within a Milky Way potential while recovering key kinematic and structural properties, offering a practical approach to connecting simulations with observations. However, reliably reconstructing the orbital history of the MCs that models their interactions accurately and reproduces their current positions, velocities, and substructures remains challenging and elusive. In particular, their close interactions are challenging to model analytically because of the strong dynamical friction and tidal distortions.

Here, we attempt to tackle the challenge of recovering the complex recent interaction history of the MCs as well as their stellar substructures with a large suite of N-body simulations. In Section 2, we discuss the *Gaia* and APOGEE data sets used for observational comparison. The simulations are described in Section 3 and details of setting up the interactions and genetic algorithm are provided in Section 4. A detailed comparison of our simulations with observed features is given in Section 5. Finally, we discuss the implications of our work in Section 6 and provide our conclusions in Section 7.

2 DATA

The observational data we use to generate the MC proper motion and density maps come from *Gaia* EDR3 (Gaia Collaboration 2021a), while the radial velocity measurements come from SDSS-IV/APOGEE DR17 (Abdurro'uf et al. 2022). To filter the *Gaia* data, we use a process similar to what is described by V. A.

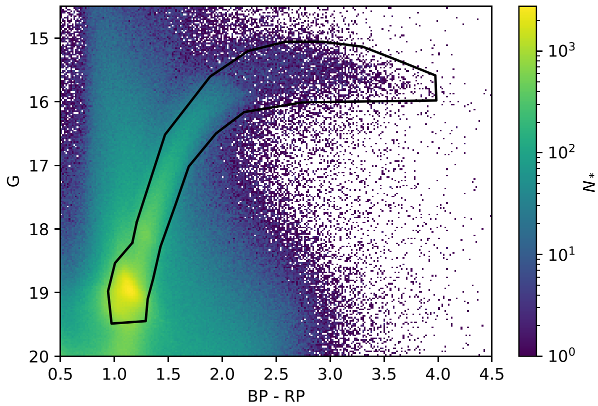

Figure 1. Colour–magnitude diagram of *Gaia* EDR3 MC stars. The black boundary shows the cuts we use for MC red clump and red giant branch stars.

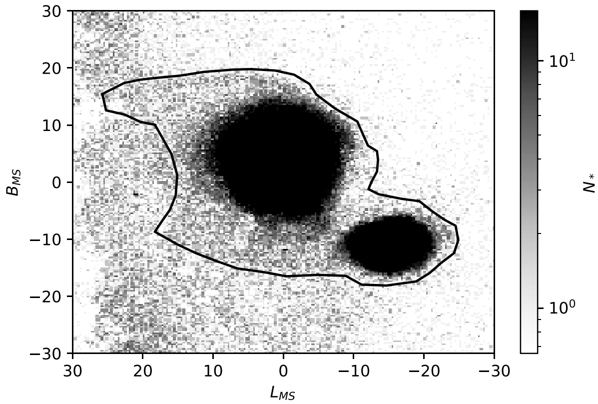

Figure 2. Density map of *Gaia* MC giant stars. The black line shows the selection we used on the map of the stars on Magellanic Stream coordinates $L_{\rm MS}$ and $B_{\rm MS}$.

Belokurov & D. Erkal (2019). A CMD filter is applied to select MC red clump (RC) and red giant branch (RGB) stars, as shown in Fig. 1. In addition, stars with proper motions outside the range of $0.9 \leq \mu_{L_{\rm MS}} \leq 2.8\,{\rm mas\,yr^{-1}}$ and $-0.6 \leq \mu_{B_{\rm MS}} \leq 1.4\,{\rm mas\,yr^{-1}}$ are removed, where $\mu_{L_{\rm MS}}$ and $\mu_{B_{\rm MS}}$ are proper motions in the Magellanic Stream (MS) coordinate system (D. L. Nidever et al. 2008). Foreground stars are also removed with a parallax cut $\varpi > 0.2$. Finally, we select stars in $L_{\rm MS}$–$B_{\rm MS}$ space to include the main stellar features of the interaction between the MCs (see Fig. 2). The observational maps of density, proper motions, and radial velocities are shown in Fig. 3.

3 SIMULATIONS

We model the interactions between the MW and MCs using N-body simulations evolved with the PKDGRAV software package (J. G. Stadel 2001). PKDGRAV is a highly efficient, fully parallel N-body code for cosmological simulations that uses a binary *k*-dimensional tree as a hierarchical representation of mass distribution. Despite being designed for cosmological simulations, PKDGRAV is also excellent for tailored N-body simulations of individual and interacting systems. Low-resolution simulations are used with the genetic algorithm for improved speed. Subsequently, a variety of higher-resolution simulations are performed for the best-fitting orbit.

For the low-resolution N-body simulations used with the genetic algorithm, the three galaxies are initialized as follows: The LMC is modeled with 1.62×10^5 star particles and 2.38×10^5 dark matter particles. The assumed stellar mass of the LMC is 7.20×10^9 M$_\odot$ and the dark matter halo has a mass of 1.76×10^{11}M$_\odot$ (D. Erkal et al. 2019). The stellar mass is higher than the observed value of 2.7×10^9M$_\odot$ (G. Besla 2015) because it includes the gas mass as well as mass that has been stripped from the LMC in the past few Gyr. The SMC has 2.25×10^4 star particles and 2.9×10^4 dark matter particles. Its stellar mass is 1.06×10^9 M$_\odot$ and its dark matter halo is 2.02×10^{10}M$_\odot$ (G. Besla et al. 2012). The MW has 2.4×10^4 star particles and 2.5×10^4 dark matter particles. Its stellar mass is 5.25×10^{10} M$_\odot$ and its dark matter halo has mass 1.16×10^{12}M$_\odot$. These three models are each evolved in isolation for 6 Gyr. The 'evolved' galaxies are then used as inputs for the genetic algorithm simulations where all three combined are run for another 2.5 Gyr.

After running the genetic algorithm, we use 10× higher resolution LMC, SMC, and MW models. The higher resolution makes it easier to find features in the MCs while having minimal effect on the orbits. In simulations comparing the orbits of the LMC with the lower and higher resolution MWs, the final LMC locations are less than 2 kpc apart.

In addition to our fiducial high-resolution LMC model (model A), we run the simulation with the same initial positions and velocities for five other LMC models: B, which has a thicker disc, C, which has a thinner disc, D, which has a hotter disc, F, which has a more compact dark matter halo, and G, which has a more diffuse dark matter halo. The properties of these models and the SMC model are given in Table 1.

4 METHODS

We run simulations with just the LMC and SMC, as well as simulations that include both MCs and the MW. For both groups of simulations, we save snapshots every 20 Myr and calculate the median particle position and velocity for the LMC and SMC. The median is used rather than the centre of mass (COM) because it is less sensitive to outliers. We compare these values to the observed COM positions and velocities shown in Table 2. The LMC velocity comes from N. Kallivayalil et al. (2013) and the SMC velocity comes from P. Zivick et al. (2018).

In both groups of simulations, we use a genetic algorithm in which we vary the initial positions, velocities, and orientations of the simulated MCs and compare them to the observed COM positions and velocities, as well as density, proper motions in the $L_{\rm MS}$ and $B_{\rm MS}$ directions, and radial velocities at the 'current' time. The current time is defined when the LMC centre reaches $L_{\rm MS}$=0°, with the Sun at the position of $(X, Y, Z) = (-8.0$ kpc, 0.0 kpc, 0.0 kpc) in the MW-centric frame.

4.1 Genetic algorithm

We employ a genetic algorithm to thoroughly and efficiently explore the 12-dimensional parameter space of initial conditions that produce the best-fitting final LMC/SMC positions and velocities. A genetic algorithm is a stochastic optimization technique that explores parameter space by mimicking natural selection, evolving a population of candidate solutions through operations such as mutation, crossover, and selection to efficiently converge

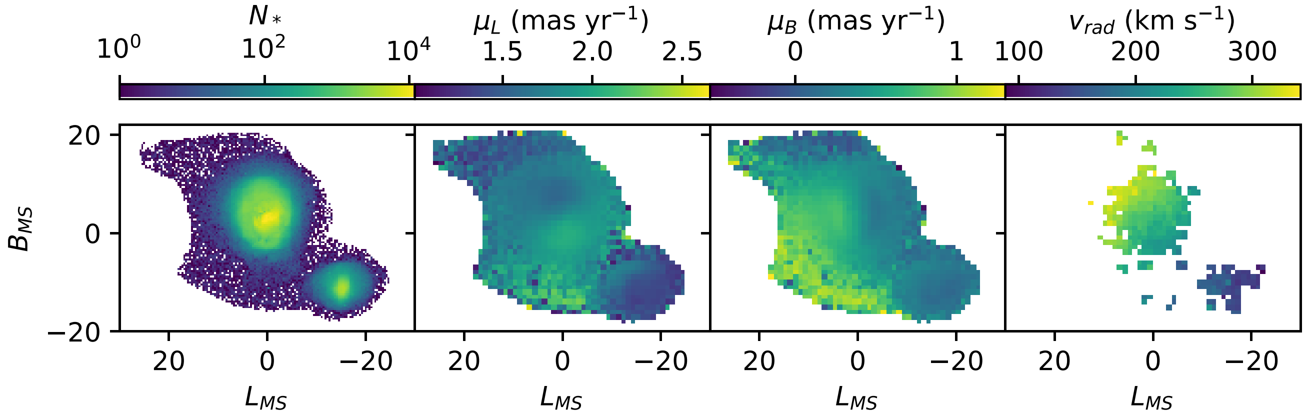

Figure 3. Maps of the observed *Gaia* and SDSS MC data. *Left:* number of stars, *centre left:* mean proper motion in the $L_{\rm MS}$ direction, *centre right:* mean proper motion in the $B_{\rm MS}$ direction, and *right*: mean line-of-sight velocity.

Table 1. Properties of the different LMC models and the SMC model we use, including halo mass M_h, half-light radius R_h, halo velocity dispersion σ_h, disc mass M_d, disc scale length R_d, disc scale height Z_d, and stellar radial velocity dispersion σ_R.

Model	M_h	R_h	σ_h	M_d	R_d	Z_d	σ_R
	(10^{11} M$_\odot$)	(kpc)	(km s^{-1})	(10^9 M$_\odot$)	(kpc)	(kpc)	(km s^{-1})
LMC A	1.76	21.4	222	7.20	2	0.28	45
LMC B	1.75	21.4	222	7.20	2	0.41	45
LMC C	1.77	21.4	222	7.20	2	0.22	45
LMC D	1.76	21.4	222	7.20	2	0.28	56.25
LMC F	1.76	13	237	7.20	2	0.28	45
LMC G	1.76	32	216	7.20	2	0.28	45
SMC	0.202	7.3	125	1.06	1.4	0.26	20

Table 2. The observed positions and velocities that we compare to the simulations and the positions and velocities for the current snapshot of the best match simulation.

Galaxy	Observed position (x, y, z) (kpc)	Observed velocity (v_x, v_y, v_z) (km s^{-1})	Simulated position (x, y, z) (kpc)	Simulated velocity (v_x, v_y, v_z) (km s^{-1})
LMC	(−1.0, −40.9, −27.7)	(−57±13, −226±15, 221±19)	(−1.0, −42.4, −25.3)	(−46, −219, 214)
SMC	(14.9, −38.1, −44.2)	(18±6, −179±16, 174±13)	(18.2, −34.6, −31.5)	(19, −190, 182)

towards optimal or near-optimal parameters. For each 'generation' of solutions (i.e. the initial conditions), fifteen simulations are run at a time. Their 'fitness' (or goodness of fit) is calculated by comparing the simulated positions and velocities of the LMC and SMC at the current time (the snapshot nearest to when the LMC crosses the Magellanic longitude of 0) with the observed values:

$$\text{fitness} = 1/\sqrt{\Delta d^2_{\rm LMC} + \Delta d^2_{\rm SMC} + \Delta v^2_{\rm LMC} + \Delta v^2_{\rm SMC}} \quad (1)$$

where Δd and Δv are unnormalized differences in the simulated and observed 3D positions and space velocities, respectively. Simulations where the LMC and SMC have merged are down-weighted by cutting the fitness value in half for any simulations where the LMC and SMC are less than 15 kpc apart at the time the LMC crosses $L_{\rm MS} = 0$. We tested incorporating comparisons to maps of stellar density, radial velocity, and proper motion in both Magellanic longitude and latitude. However, this did not have much of an effect compared to the central positions and velocities of the galaxies.

The solutions for the next generation are produced with a combination of crossover and mutation. Two solutions are selected with weighted random sampling with a probability proportional to their fitness ('fitter' solutions are more likely to be selected for a pair) and their values averaged. Randomly distributed noise is then added to these values with a Gaussian sigma of 0.5 kpc for the LMC position, 1 km s^{-1} for the LMC velocity, 1 kpc for the SMC position, and 2 km s^{-1} for the SMC velocity. The orientation of the LMC and the galaxy masses are held fixed. The best-fitting solution of each iteration is always kept to the next iteration.

4.2 Two-galaxy simulations

Initially, we modelled the recent interactions of the MCs using simulations of just the LMC and SMC without the Milky Way, focusing on the recent close interaction. In the end, these simulations failed to provide a good match for our chosen comparison features. Therefore, we moved on to simulations that also included the MW, which are described in the next

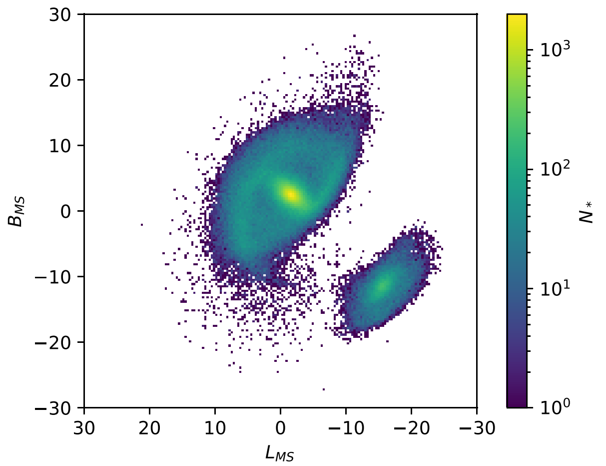

Figure 4. The LMC and SMC at the end of a two-galaxy simulation.

section. However, it is instructive to describe the two-galaxy simulations.

For our two-galaxy simulations, we centre the LMC at the start and vary the initial position and velocity of the SMC with the genetic algorithm. The two galaxies are evolved for 2 Gyr with PKDGRAV. At the end of each of simulation, the particles are translated so that the centre of the simulated LMC is at its current observed coordinates and orientation. In addition, the simulated particles are rotated about the LMC's axis so that the SMC is at its observed orientation angle from our perspective. This allows us to find the locations of the MCs as they would appear in the sky. An example of such a simulation is shown in Fig. 4.

A total of 4830 simulations were run with the genetic algorithm; however, the final solutions were not satisfactory. In simulations where the SMC ended up closest to its observed position, its velocity was never closer than 75 km s^{-1} from its observed value. We concluded that the MW's influence on the MCs was an important component that could not be approximated away by this two-galaxy approach.

4.3 Three-galaxy simulations

Next, we modelled the three-galaxy MW–LMC–SMC system with each component being 'live' and modelled as N-body star and dark matter particles. To find the initial positions and velocities for the model including the MW, we used GALA (A. M. Price-Whelan 2017; A. Price-Whelan et al. 2023) run back in time for 2.5 Gyr with MW, LMC, and SMC potentials. The potentials we used for each galaxy in GALA had the same mass for each component as we used with PKDGRAV above and matched the radial profiles as well. To accomplish this, we used a separate disc and halo component for each galaxy and adjusted their sizes and masses using the non-linear least-squares fitting function `scipy.optimize.curve_fit()` (P. Virtanen et al. 2020) to match the N-body models to a radius of 10 kpc for the disc and 50 kpc for the halo. Fig. 5 compares radial potentials of our GALA potentials to the PKDGRAV N-body models. To account for dynamical friction, which is significant in the closely interacting galaxies, we used equations (8.2) and (8.7) from J. Binney & S. Tremaine (2008) to calculate the appropriate approximation to the acceleration. For calculating dynamical friction, we set the Coulomb logarithm to be

$$\ln \Lambda = -0.4. \quad (2)$$

We have dynamical friction from the MW acting on both MCs and dynamical friction from the LMC acting on the SMC.

As shown in Fig. 6, the orbits recovered with GALA are close to, but not exactly like, the orbits with PKDGRAV. Part of this disparity is due to the fact that the dynamical friction approximation fails when the MCs closely interact, while another issue is that the shape of the haloes and thus the potential wells change as the N-body simulations evolve, but stay the same with GALA. In an attempt to mitigate the difference in dynamical friction, we increased the dynamical friction on the SMC by the LMC by a factor of seven, which improved the agreement with PKDGRAV somewhat. Even with our ad hoc adjustments to the dynamical friction, the differences in the GALA and PKDGRAV orbits were significant enough that using GALA to determine the best initial conditions was not a viable solution. The increase in dynamical friction, while overall helping the orbits match those found with PKDGRAV, caused us to overestimate the later dynamical friction between the MCs, because the haloes do not strip with GALA. Therefore, we again used a genetic algorithm as with the two-galaxy simulations to find the best initial conditions. We varied the initial positions (x, y, and z) and velocities (v_x, v_y, and v_z) of both MCs.

After running each simulation, the MW is centred and all particles are rotated about the axis of the MW until the LMC is at its observed angle on the x–y plane. Then we find the snapshot in the last 500 Myr where the centre of the LMC is the closest to $L_{\rm MS} = 0\,^\circ$. This is not necessarily the snapshot with the highest fitness because it does not take the SMC into account but for the purpose of our analysis, we want the LMC to be as close to its observed location as possible. Finally, fitness is calculated based on how well both MC median positions and velocities match the observed values from Table 2.

In addition, the distances between the MCs are tracked over time including any close interactions they have. The distance versus time plot for the best match simulation is shown in Fig. 7. In the genetic algorithm, the fitness is decreased by half (made worse) for any simulations where the LMC and SMC centres end up less than 15 kpc away from each other at the snapshot with the best LMC position. This prevents the best fit from getting stuck on initial conditions that result in the LMC and SMC merging before the present time.

Once the best initial positions and velocities for the MCs were determined, we also ran a simulation that had just the MW and the LMC starting at the COM of the LMC–SMC system. This is used to compare to the three-galaxy simulation to determine which LMC substructures formed as a result of interactions with the SMC.

5 RESULTS

5.1 Comparison to observations

After running ∼8000 simulations with the genetic algorithm, we found a best match simulation and ran the same initial conditions with 10× higher resolution. A comparison between this higher-resolution best match simulation and the data is shown in Fig. 8. For the rest of this section, we consider only the best match model.

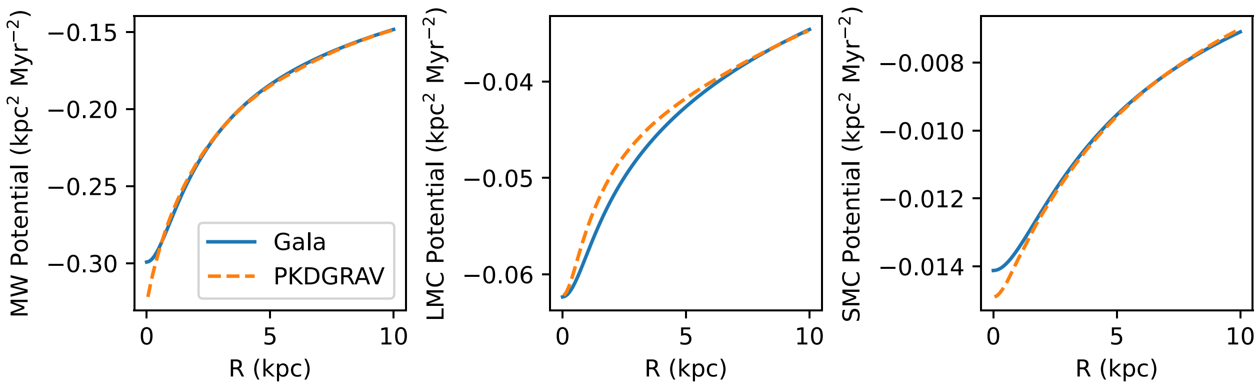

Figure 5. The potentials we use in GALA compared to the potentials of the PKDGRAV initial conditions after running in isolation for 6 Gyr.

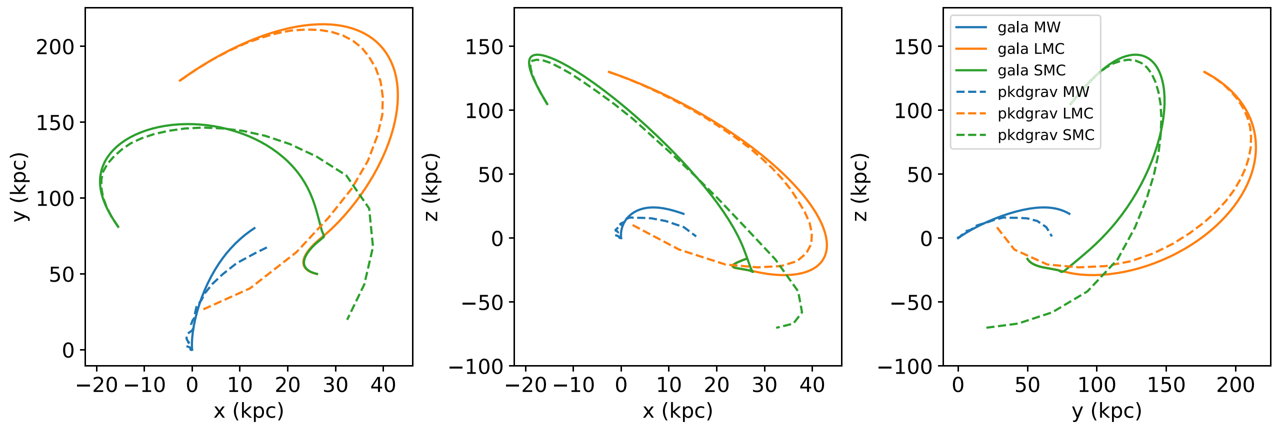

Figure 6. A comparison of orbits with GALA and PKDGRAV using the same initial conditions. The GALA orbits are shown as solid lines while the PKDGRAV orbits are dashed lines. While the orbits are fairly close at the beginning, they diverge and in the GALA run, the LMC and SMC merge. This difference could be due to the fact that with GALA, the galaxies are represented as single particles with fixed potentials, while with PKDGRAV, the shape of the galaxies and thus the shape of their potential wells can change, and stripping causes the dynamical friction and tidal forces to decrease.

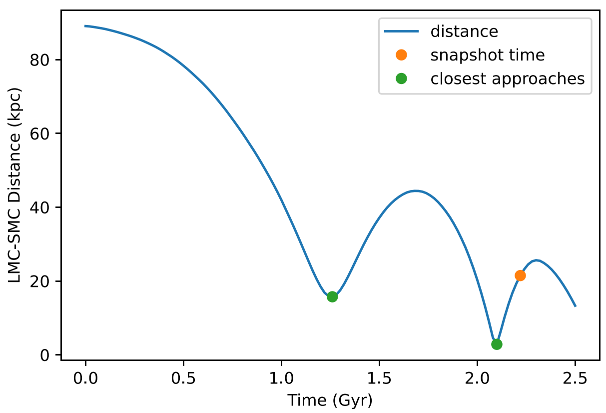

Figure 7. The distance between the LMC and SMC over time for the best match simulation. The circular markers are at the closest approaches and the triangular marker shows the time for the snapshot when the LMC crosses $L_{\rm MS} = 0°$.

Our best match simulation includes two close interactions between the LMC and SMC. The first occurred 940 Myr before the ‘current’ snapshot with an impact parameter of 15.1 kpc and the second occurred 140 Myr before the ‘current’ snapshot with an impact parameter of 3.05 kpc. When the LMC crosses $L_{\rm MS} = 0$ °, its position differs from the observed value by 2.8 kpc and its velocity is offset by 14.8 km s^{-1}. The SMC’s position differs by 13.6 kpc and its velocity is offset by 13.2 km s^{-1} from the observed values. The largest discrepancies are the SMC’s z-coordinate (offset by 12.7 kpc), the LMC’s v_x (offset by 10.8 km s^{-1}), and the SMC’s v_y (differs by 10.8 km s^{-1}). The fact that even after our extensive parameter space search the median MC positions and velocities are still offset by these non-negligible amounts shows the difficulty of finding the correct initial conditions.

Even with its shortcomings, the best-match simulation reproduces several observed features including the LMC ring, warp and northern stream. These will be explored in more detail below. Other features, such as the LMC hooks and the SMCNOD, are absent from the simulation.

5.2 LMC bar

Using the method described by W. Dehnen, M. Semczuk & R. Schönrich (2023), we can measure the length and pattern speed of the LMC bar for each snapshot. Using the threshold of Fourier amplitude $A_2 = \Sigma_2/\Sigma_0 > 0.2$ (as in M. S. Fujii et al. 2018; Ó. Jiménez-Arranz et al. 2024b), we find that the LMC formed a bar

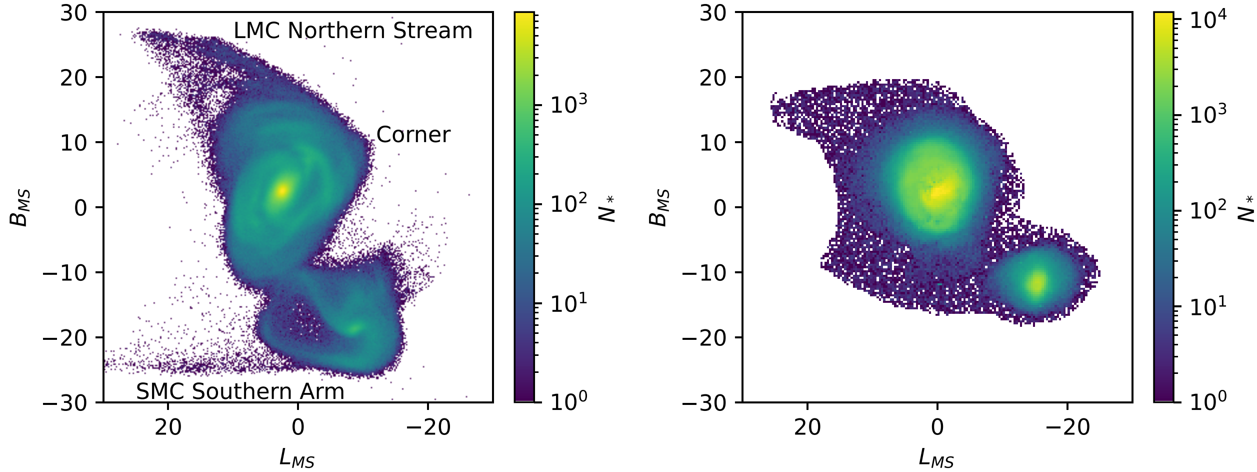

Figure 8. Comparison of density maps in MS coordinates between the best match simulation (*left*) and the *Gaia* data (*right*). Some features in the simulation are labelled.

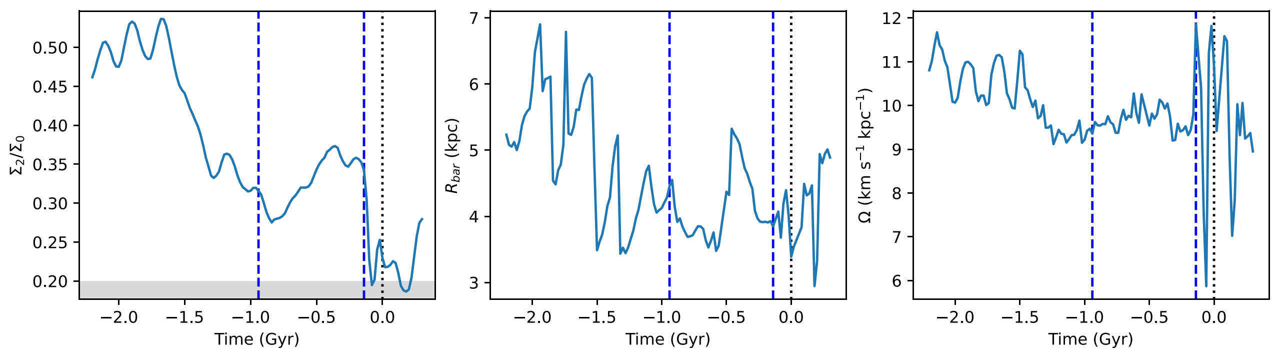

Figure 9. The evolution of the LMC bar. *Left:*A_2 for stars where $R < 5$ kpc, *centre:* the outer radius of the bar region, and *right:* the pattern speed. The dotted line is the current time, the dashed lines are the two interactions, and the shaded region in the left panel is below the threshold of 0.2 for the presence of a bar.

during the 6 Gyr it ran in isolation and the bar continues to exist for almost the entire run. Fig. 9 shows the evolution of A_2, bar length, and pattern speed over time. A_2 decreases from its initial value about 700 Myr into the run of the combined simulation. The bar experiences a small disruption after the first interaction and a larger disruption after the recent collision with the SMC, but remains above the threshold for most snapshots.

The value we use for $R_{\rm bar}$ is R_1, the outer radius of the bar region as defined by W. Dehnen et al. (2023). At the start of the combined simulation, the LMC has a bar with $R_{\rm bar} = 5.2$ kpc. This value fluctuates but tends to decrease until about 0.5 Gyr before the current snapshot, between the two interactions with the SMC. At the 'current' snapshot, $R_{\rm bar} = 3.4$ kpc, which is slightly more than the observed R_1 value of 2.3 kpc (Ó. Jiménez-Arranz et al. 2024a).

The bar pattern speed is between 9 and 10 km s^{-1} kpc^{-1} from $\sim$1.5 Gyr before the 'current' snapshot until the most recent interaction with the SMC. After the interaction, it fluctuates but the mean Ω across these snapshots is 9.6 km s^{-1} kpc^{-1}, which is similar to the value before the interaction. A range of different values for the observed LMC pattern speed have been calculated, including 11$\pm$4 km s^{-1} kpc^{-1} (N. Kacharov et al. 2024), $18.5^{+1.2}_{-1.1}$ km s^{-1} kpc^{-1} (Ó. Jiménez-Arranz et al. 2024a), and 21$\pm$3 km s^{-1} kpc^{-1} (T. Shimizu & Y. Yoshii 2012). Our value is on the lower edge of this range.

5.3 LMC ring

In our simulation, there is a high-density ring around the centre of the LMC that is similar to that described by Y. Choi et al. (2018b) using SMASH photometry of red clump stars. The ring in the simulation has a semimajor axis of approximately 7.5 kpc and a semiminor axis of approximately 5 kpc, with a position angle of $\sim$30° west of north or $\sim$150° east of north. The observed ring has a position angle of roughly $\sim$20–30° east of north and a semimajor axis of $\sim$7.5° or $\sim$7 kpc, which is similar to what is seen in the simulation. The ring is shown in a map of the LMC in Fig. 10, and the density as a function of radius for different slices of the LMC is shown in Fig. 11 (similar to the right panel of fig. 1 in Y. Choi et al. 2018b). The ring overdensity appears at radii of $\sim$4–7 kpc depending on azimuth, as expected for an elliptical ring shape. Y. Choi et al. (2018b) found that the overdensity was 2.5$\times$ higher than the underlying exponential disc at the same radius. We find that the ring overdensity in the simulation is $\sim 2.8\times$ higher.

The origin of the ring overdensity has remained unclear and Y. Choi et al. (2018b) postulated two main origin scenarios: (1) the evolution of a one-arm spiral and (2) collisionally induced by a closer recent interaction with the SMC. The ring in our simulation is made up of two spiral arms. These arms first became apparent after the first interaction with the SMC, about 1

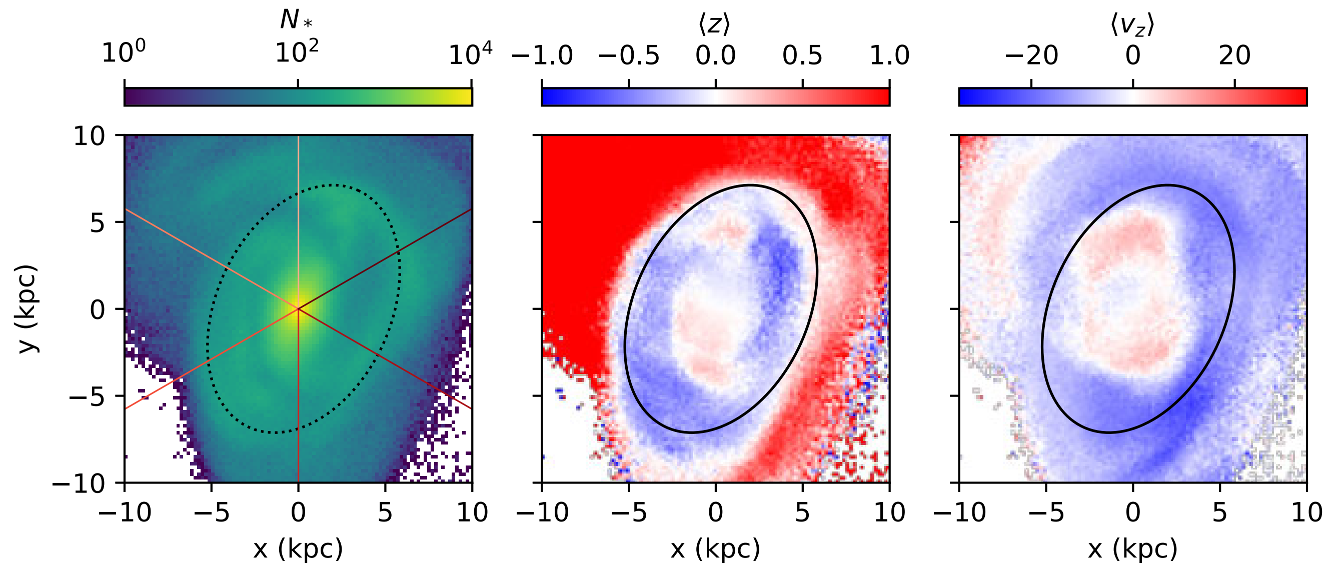

Figure 10. A face-on view of the simulated inner LMC disc and ring, coloured by *left*: density, *centre*: mean z, and *right*: mean V_z. The left panel is divided into six slices in position angle ϕ.

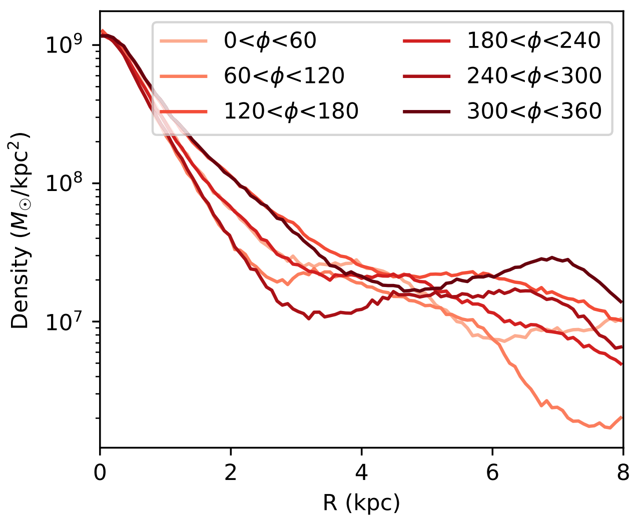

Figure 11. The mass density of the LMC disc as a function of radius in the disc plane for six slices in ϕ, the angle counterclockwise from the positive y-axis. The ring overdensity shows up at radii of 4–7 kpc depending on the position angle.

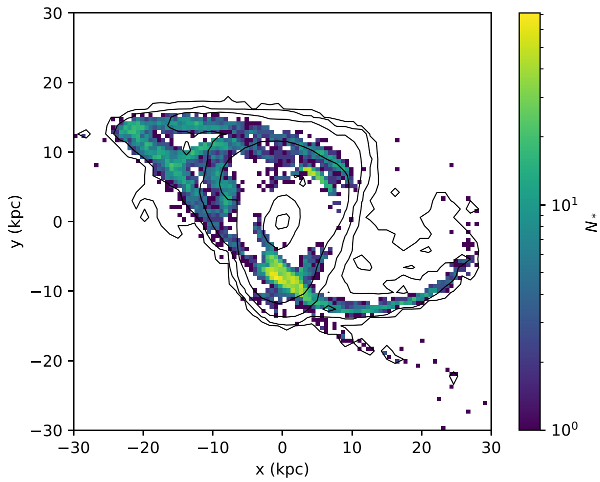

Figure 12. The face-on map of the LMC stars with a deviation value greater than 20. The deviation is a measure of how the velocity differs from the median velocity of stars at a similar radius. The contour lines show the shape of the whole LMC.

Gyr ago. After the second interaction, 140 Myr ago, these two arms overlapped temporarily, creating the ring-shaped overdensity. In future snapshots, the ring expands until the two spiral arms that comprise it separate. Then the current ring disappears, though another smaller ring temporarily forms at the centre of the LMC. The LMC ring, therefore, can be added to the mounting evidence of a recent, close encounter of the LMC and SMC.

5.4 LMC kinematic substructure

There are several signatures of LMC kinematic substructure in the simulation. To detect these substructures, we use the following procedure. The median (μ_V) and robust rms (σ_V) values of the three velocity components (V_R, V_ϕ, and V_z) are measured in 1 kpc radial bins out to a radius of 12 kpc. A ‘deviation’ value is then calculated for each star to determine how deviant its kinematics are from the bulk of the disc at its radius:

$$\mathrm{deviation} = \sqrt{\left(\frac{V_R - \mu_{V_R}}{\sigma_{V_R}}\right)^2 + \left(\frac{V_\phi - \mu_{V_\phi}}{\sigma_{V_\phi}}\right)^2 + \left(\frac{V_z - \mu_{V_z}}{\sigma_{V_z}}\right)^2}. \tag{3}$$

Stars in the main disc following normal orbits should have small deviation values, while kinematic substructures should have larger values. The map of stars that have a deviation over 20 is shown in Fig. 12.

Two distinct features are apparent in this map: (1) thin loops in the northeast and (2) a spiral arm in the southwest that extends several kpc beyond the main disc to the west. The latter was

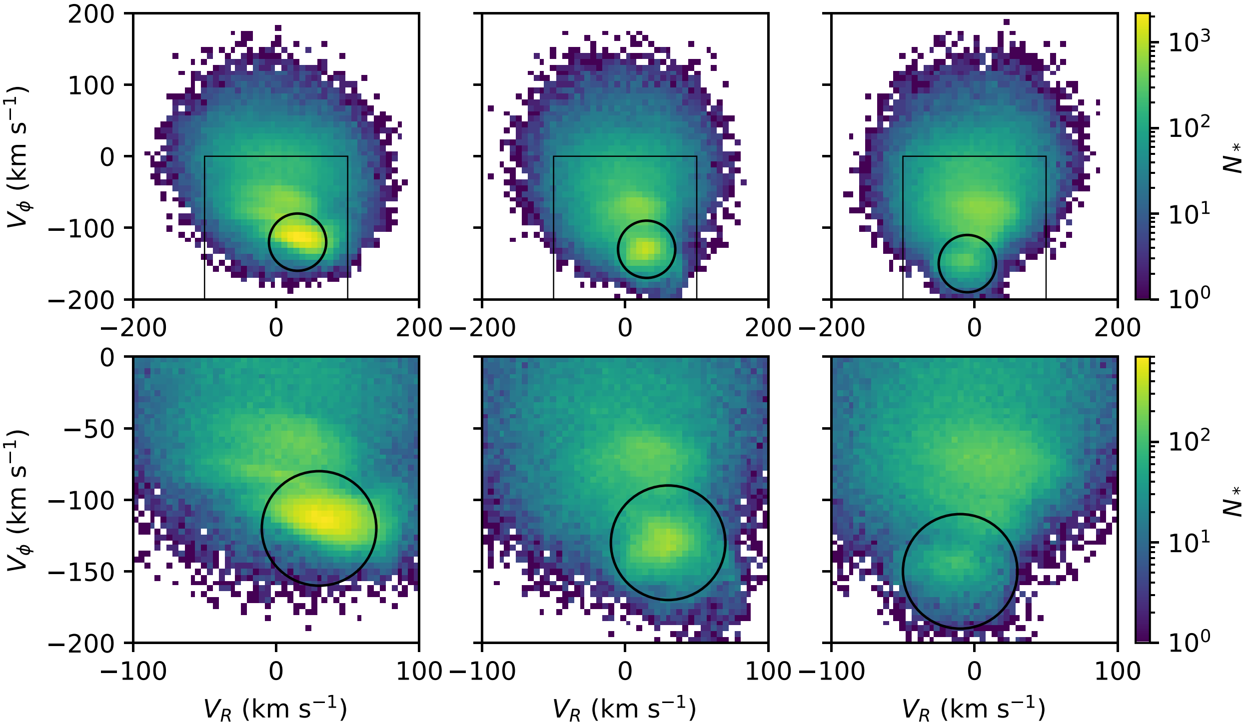

Figure 13. Plots of v_ϕ versus v_R for three different angle bins in the LMC (*left:* 30°–60°, *centre:* 60°–90°, *right:* 90°–120°). Circles show an overdensity that changes location on the plot for different angles on the LMC. The bottom row shows the same plots zoomed into the boxes in the above row.

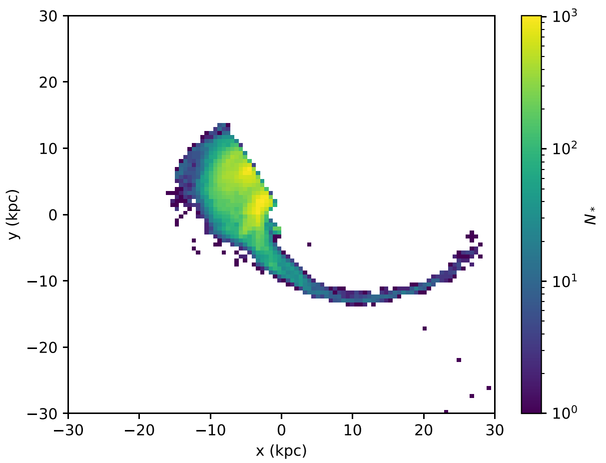

Figure 14. The combined stars of a kinematic feature of the LMC found through two different methods. The stars at negative x and $y \gtrsim -10$ are from the circled regions in Fig. 13 and rest of the stars are kinematic outliers from Fig. 12.

pulled out by the SMC during their most recent interaction. This tidal arm is remarkably thin and, therefore, also kinematically 'cool' with a velocity dispersion of only $\sim$25 km s^{-1}. Note that this feature is not visible in the map of the entire simulation in the left panel of Fig. 8 because it is hidden 'behind' the SMC.

We employ a second technique to investigate kinematic substructure. When plotting the different cylindrical velocity components against each other for a limited azimuthal range, there is an angle-dependent overdensity at high $|v_\phi|$. Fig. 13 shows this overdensity for three different eastern azimuthal slices. This feature combined with the arm mentioned in the previous paragraph forms one spiral arm as shown in Fig. 14. This is also clear from looking at the different components of velocity versus angle ϕ in the LMC disc in Fig. 15.

While there are several observed LMC substructures in the northeast that could correspond to what we see in the simulation, there is no clear observed counterpart to the western thin tidal arm. The closest possible match is the southern arm that V. A. Belokurov & D. Erkal (2019) suggest was tidally induced by the MW and SMC.

5.5 LMC northern stream

Our simulation has two arms in the northern LMC that appear in the map of kinematic features in Fig. 12. The northern stream begins at the northwest corner of the LMC and extends to the northeast corner. There is a stream of stars in a nearly straight line from the northeast corner past the southern part of the LMC in Fig. 12 that is kinematically similar to the northern stream.

A northern stream also exists when we run the simulation without the SMC (see Fig. 16), which suggests that the stream formed at least partially as a result of the interaction between the LMC and the MW. It is likely that the extra influence of the SMC enhances the northern stream.

At the western end of the northern stream, there is a 'corner'-like feature where the arm bends at a sharp angle. This is the location where the SMC impacted the LMC during their most recent interaction. The corner does not appear in the simulation without the SMC, as shown in Fig. 16. In the observed LMC, the western side is truncated (D. Mackey

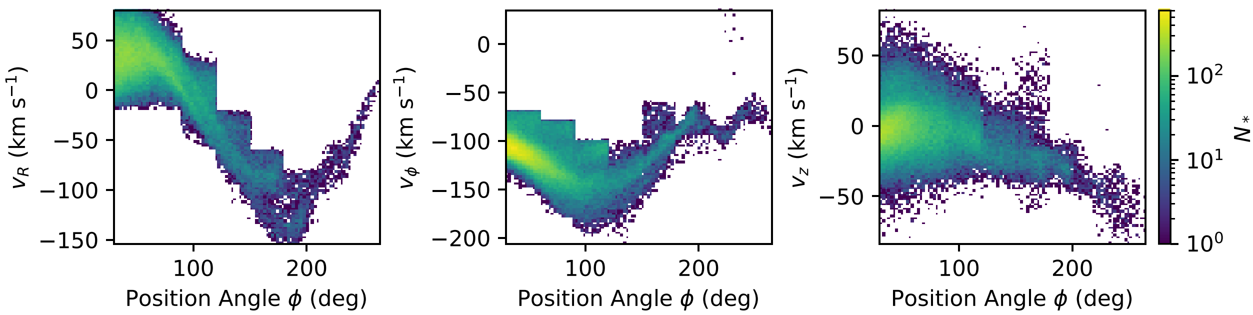

Figure 15. The velocity components versus position angle of the feature mapped in Fig. 14.

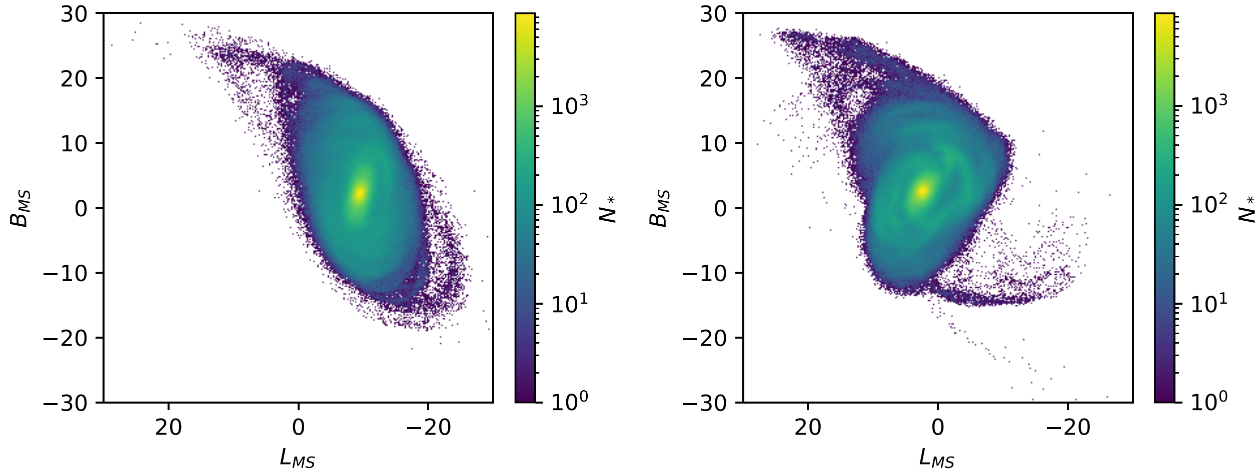

Figure 16. The LMC plotted on Magellanic Stream coordinates in simulations which exclude (*left*) and include (*right*) the SMC.

et al. 2018), which causes a slight corner in the northwest. This is visible in the northwestern part of the LMC in Fig. 2.

To compare the in-plane radial velocity of our simulated northern stream to observations, we plot the LMC on the sky, and measure the distance in degrees along the arm from where it separates from the rest of the LMC. The comparison to L. R. Cullinane et al. (2022) is shown in Fig. 17. For much of the arm, the magnitude of the velocity is less than observed but the general trend of the velocity being negative and the magnitude increasing at first then decreasing gradually along the arm is similar. Towards the end of the arm in the simulation, the in-plane radial velocity crosses into positive values. J. Wang, F. Hammer & Y. Yang (2022) also reproduced the LMC's northern stream.

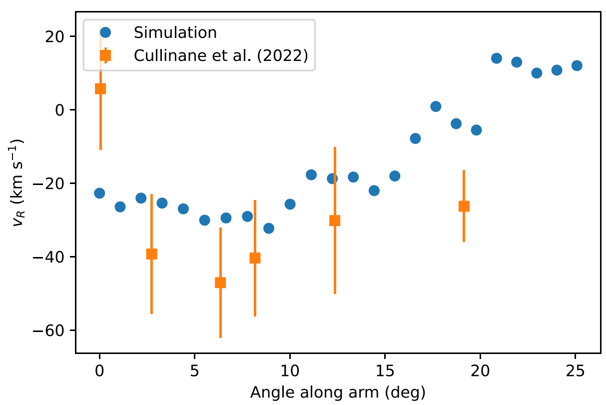

Figure 17. The in-plane radial velocity at different points along the length of our simulated northern stream compared to that measured by L. R. Cullinane et al. (2022).

5.6 LMC disc warp and vertical oscillations

In the high-resolution simulation, the LMC disc has a warp with vertical 'ripples' in the outskirts that appear after the most recent interaction with the SMC. At 140 Myr after the interaction, the warp in the LMC outskirts is above the disc plane (closer to the Sun), as defined by the central LMC, while at 300 Myr after the interaction the LMC warp is below the disc plane (farther from the Sun). A $\langle z \rangle$map of the LMC showing the warp and 'ripples' 140 Myr after the interaction is displayed in Fig. 18. The 'ripples' (or 'bending waves') start in the centre of the LMC and radiate outward. Fig. 19 shows the $\langle z \rangle$values versus X in a 2 kpc 'slit' in Y as a function of time. This clearly shows the outer disc oscillating vertically with time. Roughly half of a vertical oscillation occurs in 300 Myr indicating the period is ∼600 Myr.

Y. Choi et al. (2018a) detected a southwestern warp in the LMC at a radius of 7° and extending to 4 kpc below the LMC midplane. Later, S. Saroon & S. Subramanian (2022) detected the northern

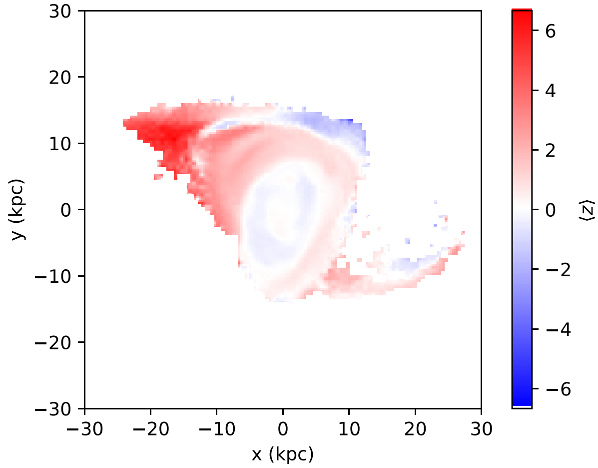

Figure 18. Face-on map of the LMC showing the 'ripples' in the disc.

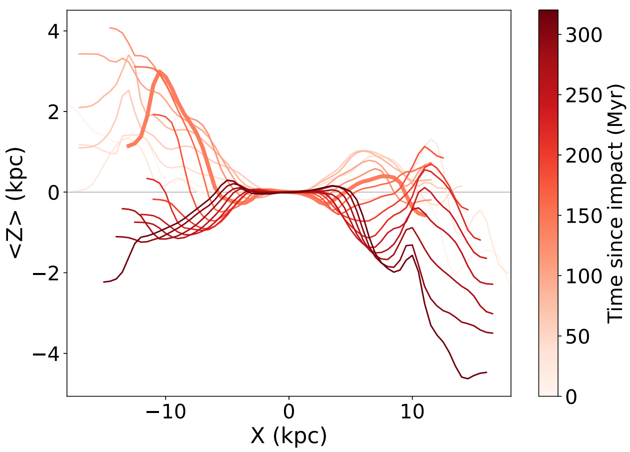

Figure 19. Vertical oscillations in the LMC disc. Mean z values versus X in a narrow 2 kpc Y-slit for the 340 Myr after the most recent LMC–SMC collision. The thicker line indicates the current time. The vertical oscillations are clearly seen.

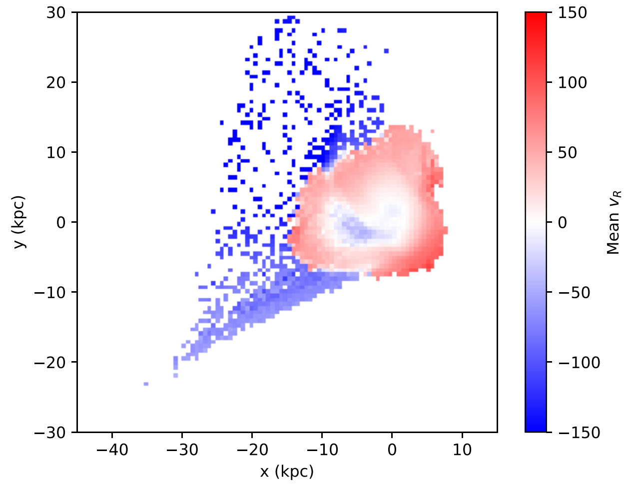

Figure 20. Face-on map of the SMC coloured by mean v_R. Most of the stars in the SMC have positive v_R increasing with radius while the stars that have been pulled away from the main galaxy tend to have negative v_R.

component of the warp (towards the northeast) at a radius of 7° and extending 1.2 kpc below the LMC midplane, in the same direction as the southern warp. Tidal interactions generally create S-shaped warps (e.g. A. Toomre & J. Toomre 1972), therefore, the detected U-shaped warp was somewhat unexpected. However, the U-shaped warp could be an effect of the bending waves that we detect in our simulation, which are produced in a direct collision of the LMC and SMC. The strong oscillations start around a radius of 7–8 kpc in the simulation, which is at a similar radius to the observed warps.

5.7 SMC expansion and rotation

In our Model A high-resolution simulation, the SMC radially expands after the most recent interaction with the LMC. The outward radial velocity of the stars increases with radius, as can be seen in the v_R map (Fig. 20), while the linear radial dependence can be seen more clearly in the left panel of Fig. 21. We find that the slope of v_R as a function of R to be 9.9±1.8 km s^{-1} kpc^{-1} extending to a radius of 6 kpc. The kinematic analysis of P. Zivick et al. (2021) of the SMC *Gaia* DR2 proper motions (to a radius of ∼4.5°) found a tidal expansion term of 10 ± 1 km s^{-1} kpc^{-1} in the direction of the LMC. Fig. 22 shows the tidal expansion of the SMC in the direction of the LMC in our simulation. The P. Zivick et al. (2021) result is indicated by a blue line indicating a good overall agreement.

Before the LMC–SMC close interactions, the SMC's rotation velocity is 60.5 km s^{-1} and reaches a maximum at a radius of ∼3 kpc in our simulation. After the most recent LMC–SMC impact, the SMC's rotation is diminished, but there remains a clear 'left-over' rotation in the simulation. The rotation velocity increases with radius until it reaches a maximum of ∼38 km s^{-1} at a radius of ∼6 kpc (right panel of Fig. 21). For stars at a radius of around 1 kpc, the median is about 18 km s^{-1}. This is within the range of 15–25 km s^{-1} for rotation at 1 kpc found by P. Zivick et al. (2021). The P. Zivick et al. (2021) kinematic analysis determined a maximum rotation velocity of 20 km s^{-1} reaching the maximum at 1 kpc. This is lower than the value we find in the simulation. The v/σ for the SMC remains fairly constant at ∼3.5 before the first interaction, at which point it drops to ∼2.5. At the most recent interaction, 140 Myr ago, it drops again to ∼1.0 and continues to decrease sharply from there. In the 'current' snapshot, $v/\sigma = 0.79$. This is slightly more than the observed value of $v/\sigma \le 0.6$ (J. Harris & D. Zaritsky 2006), but it reaches this value about 60 Myr after the 'current' snapshot.

5.8 SMC kinematic substructure

In the SMC, there is a substructure that can be seen in the plot of v_R versus R, shown in the left panel of Fig. 23. As shown in the centre panel of Fig. 23, the stars below the cut are mostly in two arms that start near the centre and extend out to a larger radius than the main SMC while the stars above the cut (right panel) are contained in the main body of the SMC. The stars in the arm to the south were pulled away from the SMC during the collision with the LMC, while the one to the east mostly remains within the SMC disc. The stars in the southern arm have a similar velocity in the x direction (∼110 km s^{-1}) and in the simulation continue past the main SMC after the current snapshot. While there is observed stellar substructure called the SMCSOD (P. Massana et al. 2024)

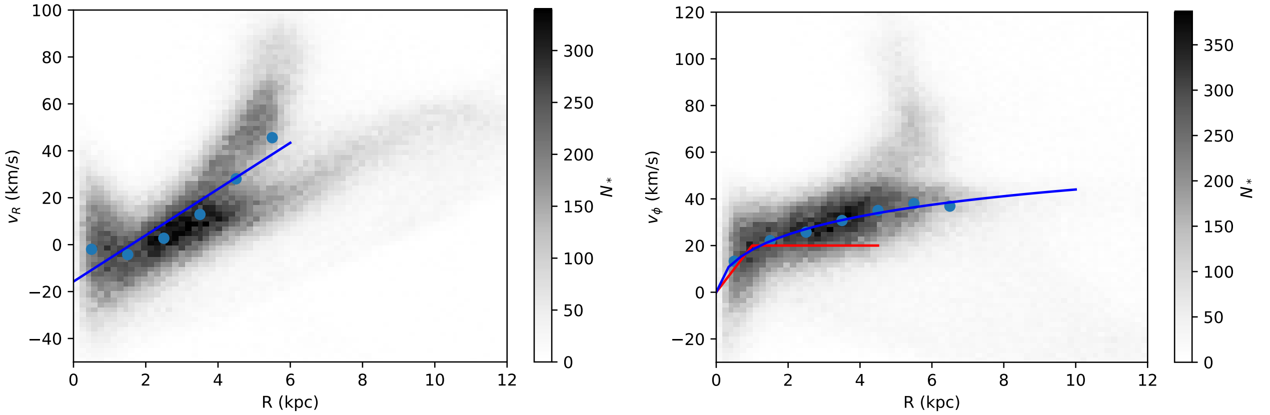

Figure 21. Kinematics of SMC star particles. Left: v_R versus R. The filled circles show the median velocity value for each of the first six 1 kpc radial bins. A linear fit of 9.9 km s^{-1} kpc^{-1} is shown by the line. Right: v_ϕ versus R. The median for each 1 kpc radial bin is again shown. A rotation curve matching the median values and the P. Zivick et al. (2021) results are also shown.

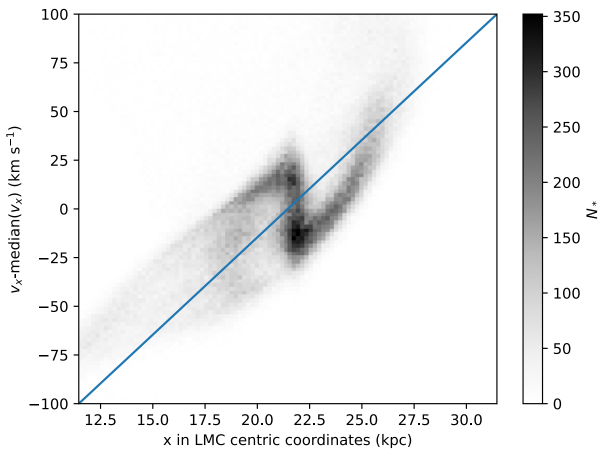

Figure 22. The tidal expansion of the SMC. The coordinate system here is centred on the LMC and the SMC is on the x-axis, so v_x is the component of the SMC's velocity towards or away from the LMC (negative is towards the LMC). The line shows the tidal expansion of 10 km s^{-1} kpc^{-1} found by P. Zivick et al. (2021).

it is as of yet unclear if these are the same structures. This feature in our simulation does not appear to be kinematically similar to the observed SMCSOD. The observed SMCSOD stars tend to have a proper motion μ_B equal to or greater than the main SMC (P. Massana et al. 2024), while in our simulation the μ_B for the stars in this feature tend to be lower than for the main SMC.

5.9 SMC stellar radial density profile

At the present snapshot, the simulated SMC disc density can be modelled as two exponentials out to a radius of 5.5 kpc, one with scale length 0.46 kpc and the other with scale length 7.87 kpc. The first models the central SMC 'core', while the second accounts for the more extended main body and tidal arms. At larger radii, the density of the SMC breaks and drops off after 5.5 kpc. The overdensity and drop-off in SMC disc density first appear ∼2 kpc from the centre about 100 Myr after the collision with the LMC and move outward, as can be seen in Fig. 24. We compare the simulation profile to the *Gaia* SMC red giant branch starcount data, which show that the SMC can be modelled fairly well with a single exponential profile for most of its extent, with a slight overdensity at a radius of ∼4–5 kpc. Observations show the SMC has a more elliptically shaped core in the inner 1–2° but is more circularly shaped at larger radii (Gaia Collaboration 2021b). These could correspond to the two components seen in the simulation. In the periphery, D. L. Nidever et al. (2011) and A. Pieres et al. (2017) both found extended SMC stellar components beyond ∼7° which in the north corresponds to the SMCNOD. There is no clear counterpart to the SMCNOD in our simulation.

5.10 SMC distance bimodality

The SMC exhibits a distance bimodality in the east, towards the direction of the LMC, which is clearly seen in the CMD distribution of red clump stars (e.g. D. Hatzidimitriou & M. R. S. Hawkins 1989; D. L. Nidever et al. 2013). The nearer group of stars, which are ∼10 kpc closer to the Sun than the main SMC, were likely separated from the SMC by tidal interactions with the LMC (A. Almeida et al. 2024). With the simulated SMC, we divide the SMC into a spatial 5×5 grid (see Fig. 25) and show their distance distributions in Fig. 26. The region where the distance bimodality is observed lies at the top of the figures at higher $B_{\rm MS}$. The central and western (bottom panels) regions show a fairly narrow single-peaked distance profile consistent with observations, while the eastern regions exhibit a clear bimodality resembling that observed. The bimodality appears after the most recent interaction between the MCs.

The eastern SMC is composed of two components. These are easily separated in azimuthal velocity in the SMC-centric frame into a prograde and retrograde component. Fig. 27 shows the spatial density of all stars and the two components in the top panels, while distance versus $B_{\rm MS}$ is shown in the bottom panels. The prograde component is more distant and has a spiral arm-like shape. In contrast, the retrograde component is closer and has the shape of a tidal arm extending from the central SMC. In addition, the stars that make up the retrograde component all come from the inner SMC (R <5 kpc). This is consistent with the results of A. Almeida et al. (2024) who found that the closer SMC component is tidally stripped from the inner SMC.

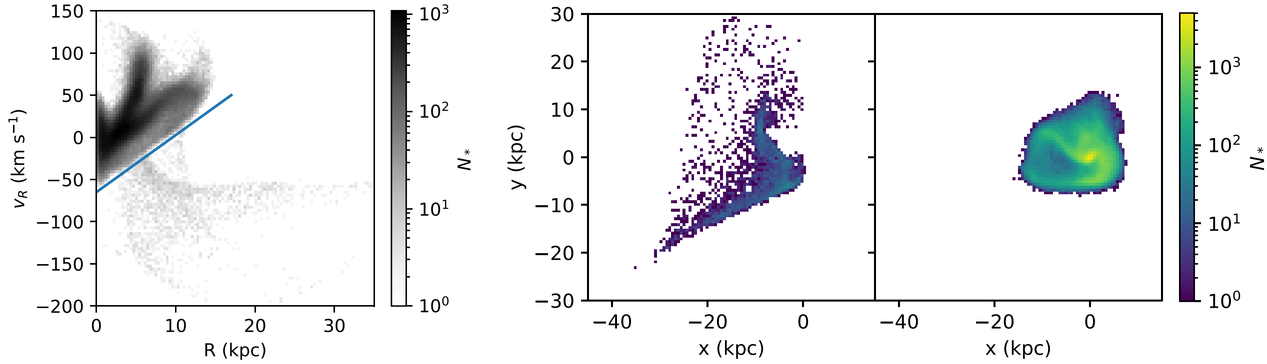

Figure 23. *Left:* MC v_R versus R with different axis limits than Fig. 21 to show stars with higher radii and negative v_R. The line is at the cutoff between the main SMC disc and a kinematic feature. *Centre:* face-on map of the stars below the v_R cut. *Right:* face-on map of the stars above that cut.

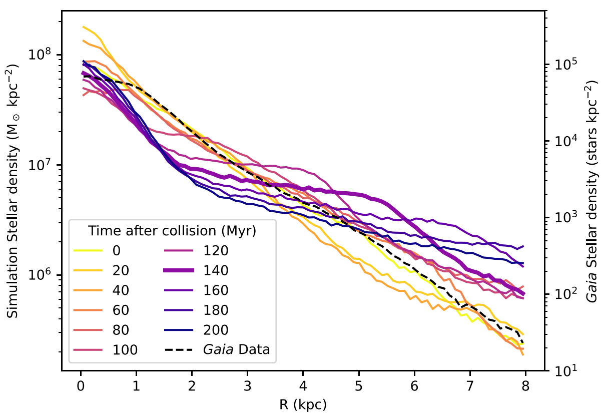

Figure 24. The radial density of the SMC for each snapshot for the first 200 Myr after the last interaction. The thicker line at 140 Myr indicates the present time and the dashed line is the *Gaia* data.

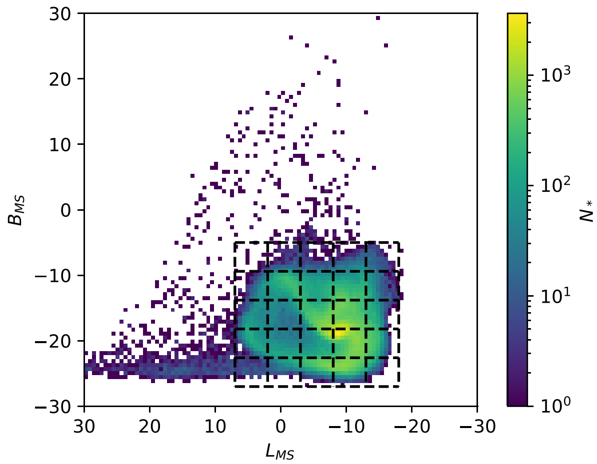

Figure 25. Map of simulated SMC stars on Magellanic Stream coordinates with dashed lines dividing the SMC into different regions. The limits of the box are $-18 \leq L_{\rm MS} \leq 7$ and $-27 \leq B_{\rm MS} \leq -5$ and it is divided into 25 equal regions. The south pole is to the left of the SMC centre in this figure, so the eastern SMC would be the upper regions, in the direction of the LMC.

5.11 Multiple LMC initial conditions

We also ran the simulation with the same starting positions and velocities but with different LMC models as described in Section 3. The maps of the different models at the 'current' snapshot are shown in Fig. 28. In all models, there are two interactions between the MCs that occur at about the same times. Every model also ends up with a northern stream, two arms forming a high-density ring in the LMC disc, and an arm pulled out from the LMC like the feature described in Section 5.4. Therefore, we conclude that these are robust features of the models.

Other things, such as the time at which the LMC crosses the MS longitude zero and the position of the SMC, differ between models. In both models, where we change the thickness of the LMC disc (B and C), as well as the one with a more diffuse dark matter halo (G), the LMC crosses MS longitude zero earlier than in the fiducial simulation. The time difference is 20 Myr in model C, 40 Myr in model G, and 80 Myr in model B. Since the timing of when the LMC crosses $L_{\rm MS} = 0$ is how we define the 'current' snapshot, it might be significant to our other results that these simulations did not run as long as the others, which had the LMC cross zero at the same time as for model A. In two of these simulations (models B and G), the location of the SMC is more directly south of the LMC than for other models. The SMC is also in a similar location (south of the LMC) in model F. In the others, the SMC is in a similar location in the sky as for the fiducial simulation.

The direction and amplitude of the warp at the 'current' time differ substantially across the models. Models A, C, and D all exhibit a positive warp (towards the Sun), with model D evolving in a way that closely mirrors model A. In contrast, models B and G have a negative warp (away from the Sun). Model F shows no coherent warp in either direction; instead, it develops only small-scale ripples. The radial extent of these ripples also varies with disc thickness. In model B, which uses the thicker disc, the ripples appear only in the outer LMC (beyond ~8 kpc). In model C, with the thinner disc, they begin much farther in, at roughly 5 kpc. Finally, the LMC disc for model G bends in both directions at different azimuths rather than forming a uniform, global warp.

Overall, the parameter that had the most effect on the simulation when changed was the concentration of the dark matter halo. The range of parameter values we looked at left much uncertainty in the characteristics of the LMC.

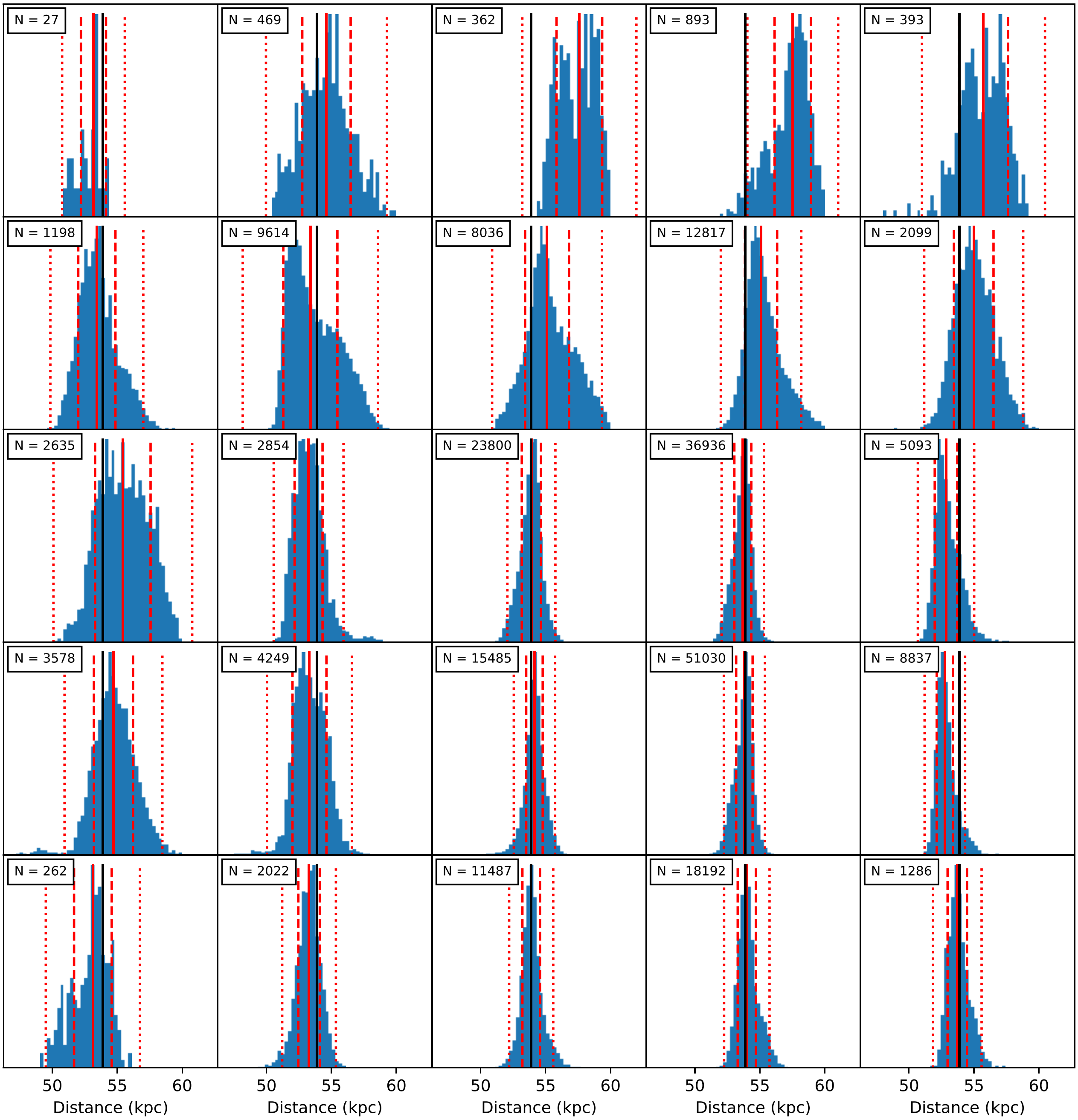

Figure 26. Normalized histograms of distances to simulated SMC stars. Each histogram is of stars in the box in the same grid location as in Fig. 25. A solid line shows the median distance, dashed lines are one median absolute deviation (MAD) away from the median, and the dotted lines are 2.5 MADs away from the median. The black line is the median distance of all the SMC stars. The MAD tends to be greater for regions in the top two rows (eastern SMC) than in the bottom three, and a bimodality is most evident in the top middle and top right plots.

6 DISCUSSION

While it is possible to 'successfully' reproduce observational results with simulations, such as the Sagittarius stellar stream by D. R. Law & S. R. Majewski (2010) and the M31 great southern stream by M. A. Fardal et al. (2013), it is generally challenging to match simulations to data. One exception is the made-to-measure technique (D. Syer & S. Tremaine 1996), which fits a system to observations by varying particle weights within a prescribed potential – an approach distinct from fully self-consistent N-body simulations and less suited to strongly non-equilibrium systems like the Magellanic Clouds. The Magellanic System is notoriously difficult to model due to the multiple strong interactions and the complexity of the system. Even with more than 8000 simulations, our genetic algorithm search of the parameter space found an approximate match to the central MC positions and velocities. Even so, there are a number of observational stellar features that are reproduced in our best-match simulation.

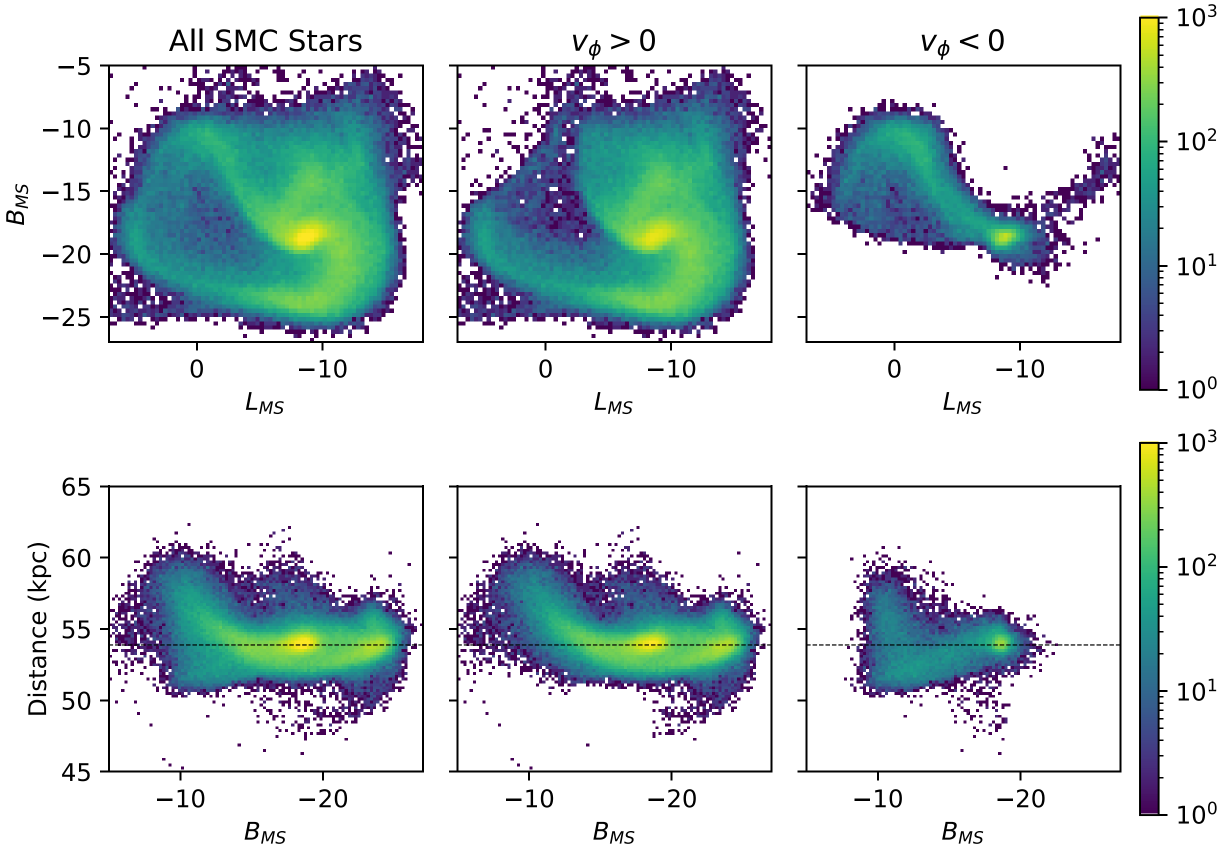

Figure 27. Density map on the sky and distance versus $B_{\rm MS}$ for simulated SMC stars. The left panels include all SMC stars, the centre panels include only the stars where $v_\phi > 0$, and the right panels include only the stars where $v_\phi < 0$. The dashed line in the bottom row is the median distance of all SMC stars.

The most recent interaction between the MCs occurred 140 Myr before the present snapshot in our simulation. This timing is consistent with the ∼140–160 Myr ago that Y. Choi et al. (2022) found. H. Rathore et al. (2025b) found that the collision likely occurred 150–200 Myr ago, which is slightly more than our estimate. The ages of the younger Magellanic Bridge stars, which likely formed as a result of the collision, also give a time range of 150–200 Myr ago (R. A. P. Oliveira et al. 2023). Our impact parameter of 3.05 kpc is less than the LMC disc size, which is in agreement with other results that suggest the most recent interaction between the MCs was a direct collision (P. Zivick et al. 2018; Y. Choi et al. 2022).

The LMC has a bar throughout the run of the simulation, which is somewhat disrupted by the recent collision with the SMC. Ó. Jiménez-Arranz et al. (2024b) also looked at the evolution of the LMC bar for N-body simulations with different parameters for the MW, LMC, and SMC. They found that the bar length and pattern speed are not significantly affected by close passages with the SMC. We also do not see much change in bar length as a result of the interactions while the pattern speed varies more between snapshots after the most recent collision. H. Rathore et al. (2025b), who used hydrodynamical simulations to model the LMC, SMC, and MW, found that the pattern speed decreases by approximately a factor of 2 after the collision with the SMC.

The LMC ring identified and characterized by Y. Choi et al. (2018b) is clearly reproduced in our simulation. While observations are unable to constrain the origin of the ring, our simulations show that it is collisionally induced by the recent direct SMC–LMC collision. The ring is made up of two overlapping arms in the LMC, and most of the stars in the ring are moving outward with a median v_R of 12.7 km s^{-1}. This ring is present in all the simulations we ran with different LMC parameters, so it is robust.

In addition, our simulation reproduces the northern LMC stream, which is a prominent observational substructure in the LMC outskirts. While V. A. Belokurov & D. Erkal (2019) were able to generate a northern stream with a simulation of only the LMC and MW, we find that the presence of the SMC significantly enhances the northern stream and modifies its shape. In our simulation, the SMC makes contact with the northwestern part of the LMC disc in the most recent interaction. This causes the northwestern edge of the stream to become substantially kinked while the western edge of the LMC disc is quite linear, similar to what is observed. Observations show that there are corresponding peaks in star formation rate in the SMC and northern LMC, suggesting that the impact point was in the northern part of the LMC disc (P. Massana et al. 2022).

The recent direct collision of the LMC and SMC also substantially affected the structure and kinematics of the SMC. The simulated SMC stars have a significant positive radial velocity component, especially beyond a radius of ∼2 kpc. This is similar to the tidal expansion observed by P. Zivick et al. (2018). Even

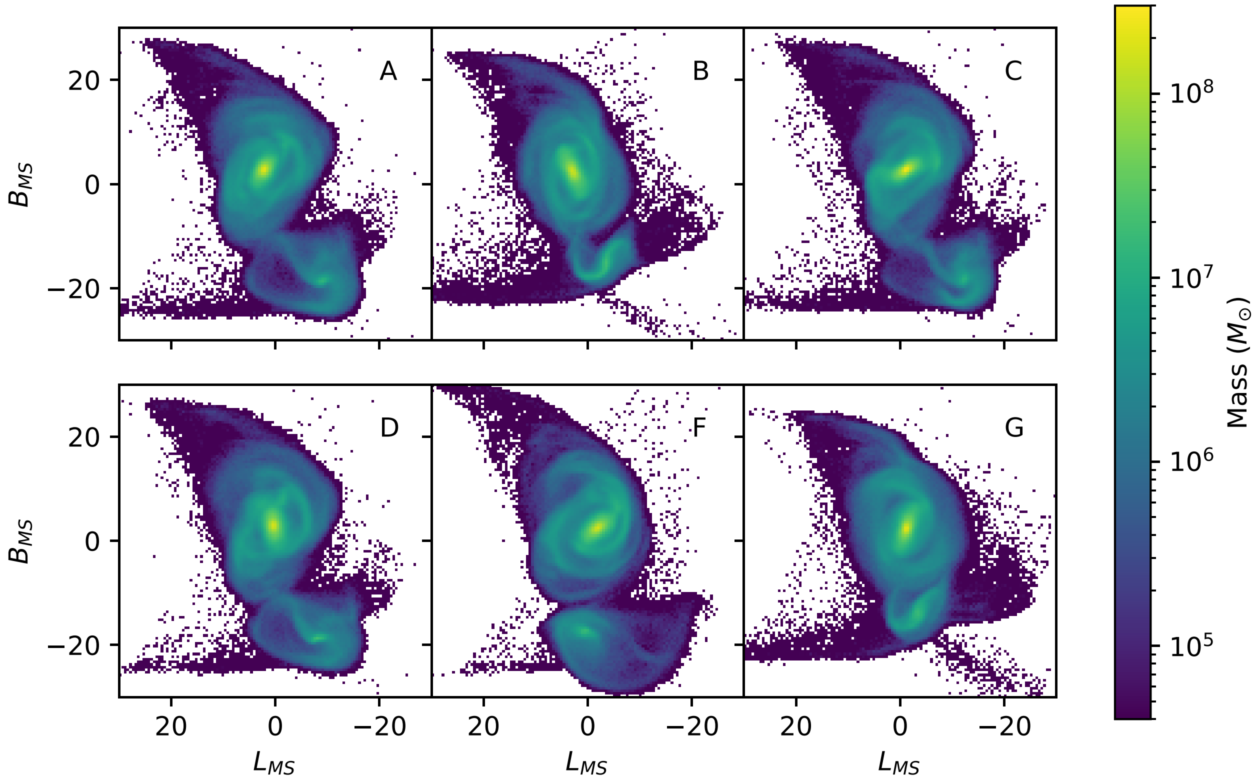

Figure 28. The maps of the different simulations at the 'current' snapshot for each model. *Top row:* models A, B, and C. *Bottom row:* models D, F, and G.

with the dramatic disturbance to the SMC's structure, it shows residual rotation at levels ∼ 2× that seen by P. Zivick et al. (2018) in the *Gaia* data.

The SMC's radial density profile changes after the collision with the LMC. Before the collision, it can be approximated as a single exponential. Shortly after the collision, there is an outward-moving overdensity that causes the inner SMC disc to be better modelled with two exponentials. H. Rathore et al. (2026) find a similar evolution of the SMC density profile 100 and 200 Myr after the collision with the LMC to what we see in our simulation.

The most pronounced SMC substructure is the distance bimodality on the eastern side. This is also found in our simulation where the eastern side of the SMC is composed of two components. The prograde component is more distant and part of the main SMC structure, whereas the retrograde component is closer and tidally pulled from the SMC centre. This confirms the findings of A. Almeida et al. (2024) which showed that the metallicity distribution function of the closer eastern component is very similar to the central SMC, while the more distant eastern component is like the western SMC periphery. C. E. Murray et al. (2024) also find a velocity bimodality in the SMC where farther away stars had a lower asymptotic rotational velocity. We find the opposite in our simulation, with the near part having a v_f of ∼35 km s^{-1} and the farther part having a v_f of ∼48 km s^{-1}.

A striking phenomenon in our high-resolution interaction simulation is the vertical oscillations of the outer LMC disc. This is a direct result of the recent collision of the two galaxies. These oscillations appear in most of the simulations where we vary LMC parameters, but are less pronounced in the one with a more concentrated dark matter halo. While similar vertical oscillations have been observed in the Milky Way, which could be due to the influence of Sagittarius dwarf spheroidal and likely the LMC (e.g. F. A. Gómez et al. 2016; C. F. P. Laporte et al. 2018), such oscillations have not yet been detected in the LMC. We predict that such vertical oscillations should be observable in the LMC, especially at larger radii, if the LMC and SMC had a direct collision. The U-shaped warp detected by Y. Choi et al. (2018a) and S. Saroon & S. Subramanian (2022) could be the inner edge of the vertical oscillations. We note that S. J. Oden et al. (2025) recently discovered that the warp is indeed U-shaped and extends to a radius of ∼15 kpc.

Our simulation does not reproduce the LMC southern hooks or the SMCNOD feature. It is quite possible that these were created by interactions of the MCs 2.5 Gyr ago. In future work, we plan to start the simulations at earlier times to capture some of these events.

7 CONCLUSIONS

We use a suite of N-body simulations of the LMC, SMC, and MW system to reproduce observed stellar features in the Magellanic System. Using a genetic algorithm, we ran over 8000 simulations of the three galaxies until we found initial conditions that resulted in the MCs being close to their observed locations after two close interactions in the past 2.5 Gyr.

Our main findings are as follows:

(i) There are two close passages between the MCs in the past 2.5 Gyr. In our best simulation, they are about 940 and 140 Myr before the LMC reaches its current position.

(ii) The LMC bar is disrupted by the most recent interaction with the SMC. This interaction does not have a significant effect on $R_{\rm bar}$ but it causes the pattern speed Ω to fluctuate.

(iii) The simulation reproduces the observed LMC ring which is a temporary structure of two collisionally induced LMC spiral arms by the recent close SMC–LMC collision which are moving radially outward.

(iv) The LMC northern stream is reproduced by a combination of MW and SMC tidal forces on the LMC. The influence of the SMC enhances the feature and creates a unique kinked shape similar to what is observed.

(v) The simulated SMC exhibits radial expansion after the recent collision which is similar to the observed tidal expansion. In addition, there is residual rotation as also observed, but at a level $\sim 2\times$ higher.

(vi) The observed distance bimodality in the eastern SMC is reproduced. This is due to two eastern components, one of which is a retrograde tidal arm pulled from the central SMC and more nearby. This is consistent with recent observations of SMC abundances.

(vii) Kinematic substructures are observed in both the LMC and SMC that do not have any clear observational counterparts.

(viii) The warp in the outer LMC shows pronounced vertical oscillations from the last SMC encounter. The U-shaped warp is consistent with observational results of the southern and northern warps in the LMC periphery.

(ix) Changing the thickness of the LMC disc affects the size and direction of the warp. In our simulation with the higher density LMC halo, only a small warp appears, while in the one with the lower density halo, the warp is S-shaped rather than U-shaped.

ACKNOWLEDGEMENTS

BRG and DLN acknowledge support from National Science Foundation grants AST 1908331 and 2408159.

We thank the anonymous referee whose comments helped us improve the manuscript.

Computational efforts were performed on the Tempest High Performance Computing System, operated and supported by University Information Technology Research Cyberinfrastructure (RRID:SCR_026229) at Montana State University. Some simulations were also run on the Flatiron Institute's Rusty computing cluster, which is supported by the Simons Foundation. Additional early simulations were run at the High Performance Computer Facility of the University of Lancashire.

Portions of the text were refined with the assistance of OpenAI's ChatGPT (GPT-5), which was used to improve clarity, grammar, and style.

DATA AVAILABILITY

Our fiducial simulation is available at https://doi.org/10.5061/dryad.1vhhmgr82

REFERENCES

Abdurro'uf et al., 2022, ApJS, 259, 35
Almeida A. et al., 2024, MNRAS, 529, 3858
Andrae R., Rix H.-W., Chandra V., 2023, ApJS, 267, 8
Barger K. A., Haffner L. M., Bland-Hawthorn J., 2013, ApJ, 771, 132
Belokurov V. A., Erkal D., 2019, MNRAS, 482, L9
Besla G., 2015, preprint (arXiv:1511.03346)
Besla G., Kallivayalil N., Hernquist L., Robertson B., Cox T. J., van der Marel R. P., Alcock C., 2007, ApJ, 668, 949
Besla G., Kallivayalil N., Hernquist L., van der Marel R. P., Cox T. J., Kereš D., 2012, MNRAS, 421, 2109
Binney J., Tremaine S., 2008, Galactic Dynamics: Second Edition Princeton University Press, Princeton, NJ
Brüns C. et al., 2005, A&A, 432, 45
Carrera R., Gallart C., Hardy E., Aparicio A., Zinn R., 2008, AJ, 135, 836
Chandra V. et al., 2023, ApJ, 956, 110
Chisholm R., D'Onghia E., Libeskind N., Lucchini S., Fox A. J., Steinmetz M., 2025, ApJ, 993, 67
Choi Y. et al., 2018a, ApJ, 866, 90
Choi Y. et al., 2018b, ApJ, 869, 2
Choi Y., Olsen K. A. G., Besla G., van der Marel R. P., Zivick P., Kallivayalil N., Nidever D. L., 2022, ApJ, 927, 153
Connors T. W., Kawata D., Gibson B. K., 2006, MNRAS, 371, 108
Cullinane L. R., Mackey A. D., Da Costa G. S., Erkal D., Koposov S. E., Belokurov V., 2022, MNRAS, 510, 445
Dark Energy Survey Collaboration, 2016, MNRAS, 460, 1270
Dehnen W., Semczuk M., Schönrich R., 2023, MNRAS, 518, 2712
Diaz J. D., Bekki K., 2012, ApJ, 750, 36
Erkal D. et al., 2019, MNRAS, 487, 2685
Fardal M. A. et al., 2013, MNRAS, 434, 2779
Filipovic M. D. et al., 1998, A&AS, 127, 119
Fujii M. S., Bédorf J., Baba J., Portegies Zwart S., 2018, MNRAS, 477, 1451
Gaia Collaboration, 2021a, A&A, 649, A1
Gaia Collaboration, 2021b, A&A, 649, A7
Gómez F. A., White S. D. M., Marinacci F., Slater C. T., Grand R. J. J., Springel V., Pakmor R., 2016, MNRAS, 456, 2779
Hagen L. M. Z., Siegel M. H., Hoversten E. A., Gronwall C., Immler S., Hagen A., 2017, MNRAS, 466, 4540
Harris J., Zaritsky D., 2006, AJ, 131, 2514
Hatzidimitriou D., Hawkins M. R. S., 1989, MNRAS, 241, 667
Jiménez-Arranz Ó. et al., 2024a, A&A, 683, A102
Jiménez-Arranz Ó., Roca-Fàbrega S., Romero-Gómez M., Luri X., Bernet M., McMillan P. J., Chemin L., 2024b, A&A, 688, A51
Kacharov N., Tahmasebzadeh B., Cioni M.-R. L., van de Ven G., Zhu L., Khoperskov S., 2024, A&A, 692, A40
Kallivayalil N., van der Marel R. P., Besla G., Anderson J., Alcock C., 2013, ApJ, 764, 161
Klein U., Haynes R. F., Wielebinski R., Meinert D., 1993, A&A, 271, 402
Kunkel W. E., 1979, ApJ, 228, 718
Laporte C. F. P., Johnston K. V., Gómez F. A., Garavito-Camargo N., Besla G., 2018, MNRAS, 481, 286
Law D. R., Majewski S. R., 2010, ApJ, 714, 229
Lin D. N. C., Lynden-Bell D., 1977, MNRAS, 181, 59
Lucchini S., D'Onghia E., Fox A. J., Bustard C., Bland-Hawthorn J., Zweibel E., 2020, Nature, 585, 203
Lucchini S., D'Onghia E., Fox A. J., 2021, ApJ, 921, L36
Lucchini S., D'Onghia E., Fox A. J., 2024, ApJ, 967, 16
Mackey A. D., Koposov S. E., Erkal D., Belokurov V., Da Costa G. S., Gómez F. A., 2016, MNRAS, 459, 239
Mackey D., Koposov S., Da Costa G., Belokurov V., Erkal D., Kuzma P., 2018, ApJ, 858, L21
Majewski S. R., Nidever D. L., Muñoz R. R., Patterson R. J., Kunkel W. E., Carlin J. L., 2009, in Van Loon J. T., Oliveira J. M., eds, Proc. IAU Symp. 256, The Magellanic System: Stars, Gas, and Galaxies. Kluwer, Dordrecht, p. 51
Majewski S. R. et al., 2017, AJ, 154, 94
Massana P. et al., 2022, MNRAS, 513, L40
Massana P., Nidever D. L., Olsen K., 2024, MNRAS, 527, 8706
Murai T., Fujimoto M., 1980, PASJ, 32, 581
Murray C. E. et al., 2024, ApJ, 962, 120
Nidever D. L., Majewski S. R., Butler Burton W., 2008, ApJ, 679, 432
Nidever D. L., Majewski S. R., Muñoz R. R., Beaton R. L., Patterson R. J., Kunkel W. E., 2011, ApJ, 733, L10
Nidever D. L., Monachesi A., Bell E. F., Majewski S. R., Muñoz R. R., Beaton R. L., 2013, ApJ, 779, 145

Nidever D. L. et al., 2017, AJ, 154, 199
Nidever D. L. et al., 2019a, ApJ, 874, 118
Nidever D. L. et al., 2019b, ApJ, 887, 115
Nidever D. L. et al., 2020, ApJ, 895, 88
Nidever D. L. et al., 2021, AJ, 161, 74
Oden S. J. et al., 2026, ApJ, 1003, 9
Oliveira R. A. P. et al., 2023, MNRAS, 524, 2244
Olsen K. A. G., Zaritsky D., Blum R. D., Boyer M. L., Gordon K. D., 2011, ApJ, 737, 29
Pieres A. et al., 2017, MNRAS, 468, 1349
Price-Whelan A. et al., 2023, adrn/gala: v1.7.1, Zenodo, https://doi.org/10.5281/zenodo.8217584 (accessed 10 October 2023)
Price-Whelan A. M., 2017, J. Open Source Softw., 2
Price-Whelan A. M., Nidever D. L., Choi Y., Schlafly E. F., Morton T., Koposov S. E., Belokurov V., 2019, ApJ, 887, 19
Putman M. E. et al., 1998, Nature, 394, 752
Putman M. E., Staveley-Smith L., Freeman K. C., Gibson B. K., Barnes D. G., 2003, ApJ, 586, 170
Rathore H., Choi Y., Olsen K. A. G., Besla G., 2025a, ApJ, 978, 55
Rathore H., Besla G., Daniel K. J., Beraldo e Silva L., 2025b, ApJ, 988, 79
Rathore H., Besla G., van der Marel R. P., Kallivayalil N., 2026, ApJ, 1000, 50
Ripepi V. et al., 2017, MNRAS, 472, 808
Růžička A., Theis C., Palouš J., 2010, ApJ, 725, 369
Saha A. et al., 2010, AJ, 140, 1719
Saroon S., Subramanian S., 2022, A&A, 666, A103
Sheng Y., Ting Y.-S., Xue X.-X., Chang J., Tian H., 2024, MNRAS, 534, 2694
Shimizu T., Yoshii Y., 2012, in Aoki W., Ishigaki M., Suda T., Tsujimoto T., Arimoto N., eds, ASP Conf. Ser. Vol. 458, Galactic Archaeology: Near-Field Cosmology and the Formation of the Milky Way. Astron. Soc. Pac., San Francisco, p. 341
Stadel J. G., 2001, PhD thesis, University of Washington, Seattle
Syer D., Tremaine S., 1996, MNRAS, 282, 223
Theis C., 1999, Rev. Mod. Astron., 12, 309
Toomre A., Toomre J., 1972, ApJ, 178, 623
van der Marel R. P., 2001, AJ, 122, 1827
van der Marel R. P., Alves D. R., Hardy E., Suntzeff N. B., 2002, AJ, 124, 2639
Vasiliev E., 2024, MNRAS, 527, 437
Virtanen P. et al., 2020, Nat. Methods, 17, 261
Wahde M., 1998, A&AS, 132, 417
Wang J., Hammer F., Yang Y., Ripepi V., Cioni M.-R. L., Puech M., Flores H., 2019, MNRAS, 486, 5907
Wang J., Hammer F., Yang Y., 2022, MNRAS, 515, 940
Wong T. et al., 2011, ApJS, 197, 16
Zaritsky D. et al., 2020, ApJ, 905, L3
Zivick P. et al., 2018, ApJ, 864, 55
Zivick P., Kallivayalil N., van der Marel R. P., 2021, ApJ, 910, 36

This paper has been typeset from a TEX/LATEX file prepared by the author.